



3D printing of piezoelectric and bioactive barium titanate-bioactive glass scaffolds for bone tissue engineering

Christian Polley^{a,*}, Thomas Distler^b, Caroline Scheufler^a, Rainer Detsch^b, Henrik Lund^c, Armin Springer^{d,e}, Dominik Schneidereit^f, Oliver Friedrich^f, Aldo R. Boccaccini^b, Hermann Seitz^{a,e}

^a Chair of Microfluidics, University of Rostock, Rostock, Germany

^b Institute of Biomaterials, Friedrich-Alexander-University Erlangen-Nuremberg, Erlangen, Germany

^c Leibniz Institute for Catalysis, Rostock, Germany

^d Electron Microscopy Centrum, University Hospital Rostock, Germany

^e Department Life, Light & Matter, University of Rostock, Rostock, Germany

^f Institute of Medical Biotechnology, Friedrich-Alexander-University Erlangen-Nuremberg, Erlangen, Germany

ARTICLE INFO

Keywords:

Bone regeneration
3D printing
Piezoelectricity
Bioactivity
Barium titanate

ABSTRACT

Bone healing is a complex process orchestrated by various factors, such as mechanical, chemical and electrical cues. Creating synthetic biomaterials that combine several of these factors leading to tailored and controlled tissue regeneration, is the goal of scientists worldwide. Among those factors is piezoelectricity which creates a physiological electrical microenvironment that plays an important role in stimulating bone cells and fostering bone regeneration. However, only a limited number of studies have addressed the potential of combining piezoelectric biomaterials with state-of-the-art fabrication methods to fabricate tailored scaffolds for bone tissue engineering. Here, we present an approach that takes advantage of modern additive manufacturing techniques to create macroporous biomaterial scaffolds based on a piezoelectric and bioactive ceramic-crystallised glass composite. Using binder jetting, scaffolds made of barium titanate and 45S5 bioactive glass are fabricated and extensively characterised with respect to their physical and functional properties. The 3D-printed ceramic-crystallised glass composite scaffolds show both suitable mechanical strength and bioactive behaviour, as represented by the accumulation of bone-like calcium phosphate on the surface. Piezoelectric scaffolds that mimic or even surpass bone with piezoelectric constants ranging from 1 to 21 pC/N are achieved, depending on the composition of the composite. Using MC3T3-E1 osteoblast precursor cells, the scaffolds show high cytocompatibility coupled with cell attachment and proliferation, rendering the barium titanate/45S5 ceramic-crystallised glass composites promising candidates for bone tissue engineering.

1. Introduction

The last few years have seen an increased interest in bioactive and smart biomaterials for hard tissue repair and regeneration. Several complex material systems have been developed by tailoring physical, chemical and biological properties to maintain control over cellular behaviour and functional tissue regeneration. Biomaterials are considered smart if they can respond to external or internal stimuli or if they possess the ability to actively stimulate or trigger effects on tissue or cells. The stimuli can vary, ranging from reactions to pH changes, temperature changes, the response to mechanical stimuli or ion

exchange [1,2]. Bioactive glasses are one of the best-known and most extensively researched examples of bioactive materials. The research field of bioactive glasses was established in 1969 by Prof. Larry Hench, who developed a glass composition of 46.1 mol.% SiO₂, 24.4 mol.% Na₂O, 26.9 mol.% CaO and 2.6 mol.% P₂O₅ (later called 45S5 Bioglass™) which created a solid bond to the bone after a short implantation time [3,4]. The rapid and strong bonding in the implant-bone interface is caused by the formation of a hydroxycarbonated apatite (HCA) layer on the surface of the glass when in contact with body fluids, induced by the dissolution of the glass and the release of ions such as calcium and phosphate ions into the interface. However, it is not only

* Corresponding author.

E-mail address: christian.polley@uni-rostock.de (C. Polley).

<https://doi.org/10.1016/j.mtbio.2023.100719>

Received 28 March 2023; Received in revised form 26 June 2023; Accepted 29 June 2023

Available online 6 July 2023

2590-0064/© 2023 The Authors. Published by Elsevier Ltd. This is an open access article under the CC BY-NC-ND license (<http://creativecommons.org/licenses/by-nc-nd/4.0/>).

the formation of an HCA layer that characterises BGs in their effect. BG, especially when provided with various dopants (e.g. Ag^+ , Cu^{2+} , Zn^{2+} , Sr^{2+} , Mg^{2+}), can trigger several beneficial biological reactions through ion release. Osteogenic [5–9], angiogenic [8–12], antibacterial [9, 13–15] and anti-inflammatory [9,16–18] properties have been demonstrated by several authors. Through targeted chemical adaptation, therapeutic effects can be induced, such as the inhibition of osteoporosis or the promotion of wound healing [9,19]. Although BG has proven its beneficial properties in various applications and has been processed in a wide variety of forms, e.g. through molding techniques, as 3D-printed ceramic scaffolds [20] or in the form of polymer-BG composites or BG fillers in hydrogels [21], they have not yet been able to replace autologous bone replacement as the gold standard.

Another interesting, smart biomaterial class that plays an increasing role in bone tissue engineering (BTE), are piezoelectric biomaterials [22–25]. Piezoelectric materials generate charges due to small deformations induced by load. The deformation of the material causes an asymmetric shift of dipoles or ions in the crystal lattice and a change in the overall electrical polarisation which generates piezoelectricity [26]. This piezoelectricity is also generated by biological tissues and seems essential in tissue development and regeneration. We already know the importance of bioelectricity in the organism in the context of neuronal signal transmission or in cardiology. But it also plays a vital role in bone and bone remodelling [27–30]. Recently, Kreller et al. showed the possibility of using biomaterials and bioelectrically stimulation to induce a cellular response to improve bone regeneration and affect bone remodelling processes [31]. Piezoelectricity in bone is achieved by collagen's highly ordered triple helix structure which exhibits an inherent polarisation. Since bone is a composite of densely packed collagen fibrils and hydroxyapatite, deformation or shearing of the collagen fibrils leads to piezoelectricity [22,32]. The collagen represents the main piezoelectric component in the bone, even though Tofail et al. demonstrated piezoelectric properties in sintered hydroxyapatite using piezo force microscopy [33]. However, the biological effects of piezoelectricity and bioelectricity orchestrating bone remodelling and regeneration continue to be discussed in the scientific community. The basic idea is that load induces deformation in the bone and generates an electric field due to the piezoelectric properties, which leads to an accumulation of ions, macromolecules and cells that then promote bone remodelling [23,24,32]. However, this theory seems to apply to dry bone mainly. In moist bone or bone in physiological environments, the piezoelectric effect cannot explain stress-generated potentials exclusively. Instead, streaming potentials, meaning potentials generated by the flow of ion-rich intestinal fluids, seem to play an important role and interact with the piezoelectric effect. In particular, a complex interplay of the streaming potential and piezoelectricity coupled via the zeta potential is being discussed. An increase in the surface charge density due to strain increases the zeta potential, thus intensifying the streaming potential and fostering bone regeneration and remodelling [22,34]. It is, therefore, reasonable to transfer the piezoelectric properties of bone to engineered biomaterials and thus, facilitate bone regeneration in a biomimicry approach. Recent studies have explored the use of lead-free piezoelectric ceramics such as barium titanate (BaTiO_3) [35–42], lithium niobate (LN) [43–45], lithium potassium sodium niobate (LNKN) [23,46,47] and potassium sodium niobate (KNN) [48,49] showing enhanced protein adsorption on charged surfaces and increased cell proliferation and metabolic activity. Therefore, combining a piezoelectric ceramic which causes autonomous stimulation of bone cells through bioelectric cues with a classical bioactive material that leads to rapid biomineralisation in the interface is quite promising. Recently, a research group led by Saeidi et al. demonstrated the beneficial properties of a freeze-casted BaTiO_3 /BG composite scaffold with high cytocompatibility and high cell viability of up to 98% compared to the control group [50]. In another approach by Zhao et al. the combination of a poly (vinylidene fluoride) (PVDF) membrane with electro-spun collagen fibres with incorporated microscale BG particles

showed promising bone regenerative results both *in vitro* and *in vivo* [51]. The increased bone healing is attributed to the increased accumulation of calcium ions on the polarised surface of the PVDF membrane. The authors found that the high concentration of Ca^{2+} simultaneously leads to increased activity of the calcium-sensing receptor of the osteoblasts and thus, further promotes osteogenesis [51, 52]. However, combining piezoelectric and bioactive materials with modern manufacturing methods such as 3D printing has not yet been studied.

In this study, we combine the advantages of piezoelectric (BaTiO_3) and bioactive (45S5® Bioglass) biomaterials in an additive manufacturing process to achieve functional, 3D biomaterials for bone regeneration. We show dense specimens and scaffolds with defined pore sizes can be produced using a binder jetting process. Through subsequent thermal post-treatment, we achieve dense composite materials with mechanical properties in the range of physiological spongy bone [53–55]. In this case, bioactive glass serves not only as a bioactive mediator but also as a matrix stabilising component: by adding bioactive glass, we significantly improved the mechanical properties of 3D-binder-jetted BaTiO_3 scaffolds compared to previously published BaTiO_3 -hydroxyapatite (BaTiO_3 /HA) composites [40]. Afterwards, we assessed the piezoelectric and bioactive properties of the fabricated scaffolds. Finally, we investigated cell adhesion and cytocompatibility of the materials toward MC3T3-E1 murine pre-osteoblast cells. As a result, the bioactive and piezoelectric multi-functional composite materials shown in this study advance the field of composite biomaterials for bone regeneration by offering scaffolds for piezoelectric and bioactive stimulation of bone cells.

2. Materials and methods

2.1. Material and fabrication

To produce a printable powder mixture, BaTiO_3 powder (d_{50} : 3,0 μm , Sigma-Aldrich/Merck KGaA, Darmstadt, Germany), 45S5 bioactive glass powder (d_{50} : $4.0 \pm 1.0 \mu\text{m}$, composition: 45 wt% SiO_2 –24.5 wt% CaO –24.5 wt% Na_2O –6 wt% P_2O_5 , Schott Vitryxx™, Schott AG, Germany) and an additional SiO_2 -based flowing agent (Aerosil R8200™) were mixed with Polyethylenmethacrylate (PEMA, DEGACRYL™, Evonik Industries, Essen, Germany) in a jar rolling mill WTR 295 W/R (Welte Mahltechnik GmbH, Ransbach-Baumbach, Germany). The powders were dried and sieved in advance to avoid any agglomerations. The exact composition of the powder mixtures is shown in Table 1. Cylindrical samples, dense and with interconnected macropores, as published previously, were designed using CAD software (SolidWorks, Dassault systems, Waltham, USA) [40]. The powder mixture was 3D-printed on a Voxeljet VX500 binder-jet printer (Voxeljet AG, Friedberg, Germany) with a layer thickness of 100 μm and a printing resolution of 250 dpi. In brief, the printer deposits a binder fluid (SOLUPOR, Voxeljet AG, Friedberg, Germany) in a layer-by-layer process according to the *.STL file, and partially dissolves the polymeric phase. The binder consists of a solvent mixture using hexane-1-ol, 2-ethylhexyl acetate, and hexyl acetate, as published in previous protocols [40,56]. After a waiting period of 24 h to ensure that the solvent evaporated, they were removed from the powder bed. Samples were stored for at least 24 h in a drying cabinet (Heraeus T6060, Hanau, Germany) at 40 °C for complete curing.

Table 1
Powder mixture compositions used for 3D printing.

	BaTiO_3	BG (45S5)	SiO_2	PEMA
BaTiO_3 /5%BG	81.8 wt%	5 wt%	1.5 wt%	11.7 wt%
BaTiO_3 /15%BG	73.2 wt%	15 wt%	1.3 wt%	10.5 wt%

2.2. Post-processing

Finding a suitable process window for sintering BaTiO₃/BG composites is critical in producing final scaffolds. BaTiO₃ is conventionally sintered at high temperatures around 1300 °C [37,57–60]. At these temperatures, BG is already present as a melt and generally loses its bioactive properties (degree of crystallinity increases) due to excessive heat treatment [61,62]. We have relied closely on existing literature on the sintering of BaTiO₃ and BaTiO₃ composites to determine the sintering curve used here and on our own research and experiments [40, 63]. After drying, the samples were thermally post-processed for 1 h at 300 °C and 2 h at 500 °C in a furnace to remove the polymer matrix. The post-processed specimens were then sintered in a furnace under an ambient atmosphere to obtain dense ceramic-crystallised glass composites. The sintering curves are visualised in Fig. 1.

2.3. Morphological and microstructural characterisation

To determine the shrinkage after sintering, the samples were measured with a digital calliper (conforms to DIN 682) before and after thermal post-processing (n = 5 per group). The density and porosity of the sintered samples (n = 5 per group) were determined with the Archimedes' principle using a specially equipped precision scale (LA230s, Sartorius AG, Göttingen, Germany). Scanning electron microscopy (SEM, Merlin VP compact, Carl Zeiss AG, Jena, Germany) and electron dispersive X-ray spectroscopy (XFlash 6/30 Co., Bruker, Berlin, Germany) were used to assess the microstructure and chemical composition. X-ray diffraction (XRD) powder patterns were recorded on a Panalytical X'Pert $\theta/2\theta$ -diffractometer equipped with an Xcelerator detector using automatic divergence slits and Cu α_1/α_2 radiation (40 kV, 40 mA; $\lambda = 0.15406$ nm, 0.154443 nm). Cu beta-radiation was excluded using a nickel filter foil. Measurements were performed with 0.086° s⁻¹, respectively. Finely pestled samples were mounted on silicon zero background holders. After data collection, obtained intensities were converted from automatic to fixed divergence slits (0.25°) for further analysis. Peak positions and profiles were fitted with the Pseudo-Voigt function using the HighScore Plus software package (Panalytical). Phase identification was done by using the PDF-2 database of the International Center of Diffraction Data (ICDD).

2.4. Mechanical characterisation

Compression tests on cylindrical samples (n = 5 per group) were performed using a uniaxial testing machine (Zwick Roell Z5.0, Zwick-Roell GmbH, Ulm, Germany) with a 5 kN load cell and a crosshead speed of 0.5 mm min⁻¹. Prior to the compression test, the top and bottom surfaces of the scaffolds were ground to achieve optimal testing conditions in a uniaxial testing state. The Young's modulus was calculated between 1.5% and 2% strain.

2.5. Poling and piezoelectric characterisation

The fabricated cylindrical samples were polarised in a strong electrical field. The polarisation setup consists of a sample holder with silver (Ag) electrodes on both sides that were connected to a high voltage power supply (HNCs 10,000–180 pos., Heinzinger, Rosenheim, Germany). The sample holder was placed in a heated silicon oil bath (ELBESIL, L. Böwing GmbH, Hochheim) to prevent any sparks and to polarise the scaffolds shortly below the Curie temperature (120 °C). The samples were polarised applying a field strength of 1.25 kV/mm for 30 min. The piezoelectric constant d_{33} was measured with the Berlincourt method [64] using a d_{33} piezometer (PM300, PIEZOTEST, Singapore). For the piezoelectric assessment n = 5 samplers per group were used.

2.6. Bioactivity testing

To investigate the bioactivity of BaTiO₃/BG composite scaffolds, simulated body fluid (SBF) was produced according to (Kokubo) and ISO 23317 [65]. 3D-printed discs with a diameter of $d = 5$ mm and $h = 2$ mm height were fabricated with n = 3 samples per group. The samples were placed in SBF according to previously published protocols [55], and placed on a shaking incubator (Heidolph Unimax 1010, Heidolph Instruments GmbH & CO. KG, Germany) at 37 °C and 90 rpm. SBF was changed every two days. Samples were removed after 7, 14, 21, and 28 days of immersion in SBF. The samples were rinsed with ultrapure water and dried under a fume hood at room temperature (22 °C, RT). Subsequently, the scaffolds were analysed by Fourier-transform infrared spectroscopy (FTIR) and SEM/EDS analyses as described elsewhere [55]. In brief, FTIR (IRAffinity-1S, Shimadzu Europa GmbH) absorbance spectra were recorded for the BaTiO₃/BG composite scaffolds before incubation in SBF and after each incubation time point. SEM (Auriga Crossbeam, Carl Zeiss Microscopy GmbH, Germany) and EDS (X-MaxN, Oxford Instruments) were used to assess the surface morphology as well as to determine the elemental surface composition of the BaTiO₃/BG scaffolds, respectively.

2.7. Cell culture studies

2.7.1. Cell culture and maintenance

Mouse calvaria pre-osteoblast cells (MC3T3-E1, Sigma Aldrich, Germany) were cultured in alpha-modified minimum essential medium (α -MEM) (Gibco®, Life Technologies™, Germany), supplemented with 10% (v/v) fetal bovine serum (FBS), 1% (v/v) penicillin/streptomycin (all Sigma-Aldrich, Germany) and 1% (v/v) L-Glutamine (Thermo Fisher Scientific Inc., USA). Cells were passaged in T75 cell culture flasks (Sarstedt, Germany) and maintained at 37 °C, 95% air, 5% CO₂ humidified atmosphere in an incubator (Galaxy® 170 R, Eppendorf AG, Germany). Trypsin/EDTA (Sigma Aldrich, Germany) was used for cell detachment, while cell counting was performed via the trypan blue

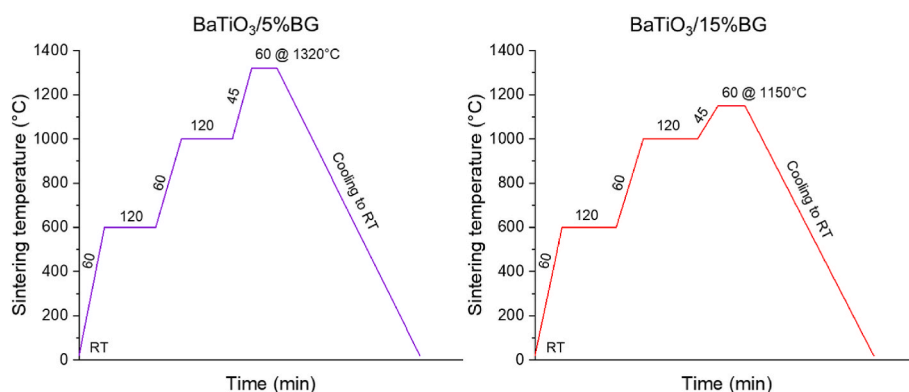


Fig. 1. Sintering curves for the respective composites BaTiO₃/5% BG and BaTiO₃/15%BG. Both were sintered with a conventional furnace in air.

exclusion method using Neubauer chambers (Paul Marienfeld GmbH & Co. KG).

To assess the cytocompatibility of 3D-printed BaTiO₃/BG and BaTiO₃/HA (as a benchmark, previously published [40]) scaffolds, 100,000 cells/ml MC3T3-E1 were seeded on 3D-printed cell culture discs (1 ml/scaffold) in 24-well cell culture plates. The samples were cultured for 24 h to assess initial cell attachment and *in vitro* cytocompatibility. Tissue culture polystyrene (TCPS) substrates served as an additional control to the 3D-printed BaTiO₃/BG discs. To assess pH change due to potential BG dissolution from the scaffolds, the cell culture medium (5 ml, n = 4 scaffolds) was removed 24 h after cell seeding, and the pH was recorded.

2.8. LIVE/DEAD staining

Cell viability was determined by performing a LIVE/DEAD staining assay as described previously [55]. After 7 days, cells were stained using calcein acetoxymethyl ester (Calcein AM, LIVE) (Invitrogen™, Molecular probes by Life technologies™, USA) and propidium iodide (PI, DEAD) (Invitrogen™, Molecular probes by Life technologies™, USA), to indicate viable and dead/apoptotic cells, respectively. BaTiO₃/BG samples were washed with phosphate-buffered saline (DPBS, Thermo Fisher, USA) and incubated with 1 ml of DPBS stock solution containing 4 μl/ml Calcein AM and 5 μl/ml PI for 45 min. Samples were washed (DPBS) and fixed using 500 μl of fixation solution (0.1 M PIPES (Piperazine-N,N'-bis(2-ethanesulfonic acid), Merck, Germany), 1 mM EGTA (Ethylene glycol tetraacetic acid, Merck, Germany), 4% (w/v) polyethyleneglycol, 3.7% (w/v) paraformaldehyde (all Sigma Aldrich, Germany) in Hank's balanced salt solution (HBSS)).

2.9. Multiphoton fluorescence microscopy

After 7 days of incubation, samples of BaTiO₃/5%BG and TCPS control (n = 3) were washed using HBSS and fixed using 4% formaldehyde solution (in HBSS) for 5 min. The cells were permeabilised (0.1% TritonX-100 for 5 min) and washed twice using HBSS. Subsequently, the cells were stained using 5 and 1 μl/ml of Rhodamine-phalloidin F-Actin/4',6-Diamidino-2-phenylindol (DAPI) (both Life Technologies, Thermo Fisher, USA), in HBSS, for 1 h and 5 min, respectively. The samples were imaged using a multiphoton microscope (TriMScope II, LaVision BioTec, Bielefeld, Germany) equipped with a HC FLUOTAR L 25x/0.95 W VISIR objective (Leica Microsystems GmbH, Germany). DAPI was excited using a mode-locked ps-pulsed Ti:Sa laser (Chameleon Vision II, Coherent, Santa Clara, USA) at 810 nm. The sample fluorescence was recorded using the following single bandpass filters: 450/30 nm (DAPI), 525/50 nm (Calcein-AM), and 620/60 nm (Rhodamine-Phalloidine), all Chroma Technology group (Acal Bfi Germany GmbH, Germany). Different photomultiplier tubes (PMT) were used for each channel. Every image had a field-of-view of 409.6 x 409.6 μm². The imaging depth was adapted according to sample roughness (TCPS, flat; 3D-printed BaTiO₃/5% BG, rough), in order to capture all cells in the field-of-view. Maximum intensity z-projections were made for a qualitative assessment. Cell number and density were quantified using ImageJ (ImageJ software package, Fiji, ImageJ 1.52i). For the analysis, n = 6 samples of BaTiO₃/BG composite and n = 3 samples of positive TCPS controls were used.

2.10. Cell material interaction

The interaction of MC3T3-E1 cells with BaTiO₃/BG scaffold surfaces was assessed using SEM. Briefly, cells were fixed after 7 days of incubation on the samples and transferred to two SEM-fixation solutions [66] for 1 h, respectively. The samples were then dehydrated using an ethanol series by subsequent incubation in 30%, 50%, 70%, 75%, 80%, 85%, 90%, 95% and 99% EtOH/H₂O solutions for 10 min each. Prior to imaging, the samples were dried using a critical point drier (EM

CPD300, Leica, Wetzlar, Germany). SEM images were recorded using an Auriga CrossBeam SEM (Carl Zeiss, Oberkochen, Germany).

2.11. Extracellular lactate dehydrogenase release assay (LDH)

To assess the potential cytotoxicity of BaTiO₃/BG scaffolds, extracellular LDH release was determined from cell culture supernatants using the TOX7 *in vitro* toxicity kit (Sigma-Aldrich). Aliquots of 500 μl were removed from MC3T3-E1 cells cultured for 24 h on TCPS, BaTiO₃/HA, BaTiO₃/5%BG, and BaTiO₃/15%BG samples (n = 6), and frozen at -21 °C until further use. All samples were treated according to the manufacturer's instructions and as described in previous studies [67]. Briefly, samples were thawed on the day of analysis and 140 μl of the supernatants were transferred into UV-vis cuvettes (path length: 10 mm, Sarstedt, Germany). LDH master-mix solution (60 μl) containing equal amounts of substrate solution, LDH cofactor solution, and dye solution were added to the cuvettes and incubated at RT for 30 min in the dark. The samples were diluted using 700 μl UPW, and the absorption was immediately measured (λ = 490 nm, 690 nm) using a UV-vis spectrophotometer (NanoDrop One, ThermoFisher, USA) in cuvette mode.

2.12. PicoGreen proliferation assay

Cells were grown for seven days on TCPS, BaTiO₃/HA, BaTiO₃/5% BG, and BaTiO₃/15%BG samples. Cells grown BaTiO₃ composites (n = 6) and TCPS controls were washed using HBSS and frozen at -80 °C to facilitate cell lysis and DNA release. On the day of the experiment, samples were thawed and washed using 1 ml of 1 × TE PicoGreen assay buffer solution (Quant-iT PicoGreen ds-DNA Assay-Kit, Invitrogen, Life Technologies, ThermoFisher, USA). Equal amounts of Quant-iT PicoGreen working solution and sample (50/50) were mixed and incubated for 3 min at RT without light. The relative fluorescence (RFU) was recorded using a CFX connect spectrofluorometer (Bio-Rad, Germany). LambdaDNA assay standard served as the calibration curve (R² = 0.99). DsDNA data for all samples were normalised to cells grown on TCPS for 24 h as a control.

2.13. Statistical analysis

All statistical analyses were performed using GraphPad Prism v9.1.0 software. Data were checked for normal distribution using Shapiro-Wilk tests. Normally distributed data were subjected to unpaired Student t-tests (Fig. 7b) for pair-wise comparisons or one-way ANOVA tests (Fig. 7c, e). Non-normally distributed data (Fig. 7d) was analysed using the Mann-Whitney test. p < 0.05 was considered as statistically significant differences between groups.

3. Results and discussion

3.1. Scaffold fabrication and morphology

Fig. 2 shows the fabrication route we used to produce bioactive and piezoelectric scaffolds. The first important step was the selection of the starting materials and preparing a homogeneous and flowable powder blend. For the piezoelectric components, we chose BaTiO₃ which is lead-free and has already shown its suitability as a biomaterial in several publications [32,35,39]. As a bioactive component, we used 45S5 Bioglass which, despite the possibility of improved bioactive glasses, is still the typical benchmark material in the context of classical bioactivity [68]. As previously described, both were mixed with polyethylene methacrylate (PEMA) to form a flowable blend [40,69,70]. Fig. 2B and C show SEM images for both powder blends BaTiO₃/BG5% and BaTiO₃/BG15%. The supplementary material section shows representative SEM images of the individual base materials (Fig. S1). The apparent difference in particle size shows microscopic BaTiO₃ particles (d₅₀ 3 μm) and much larger BG flakes (d₅₀ 20 μm). In addition, the EDS

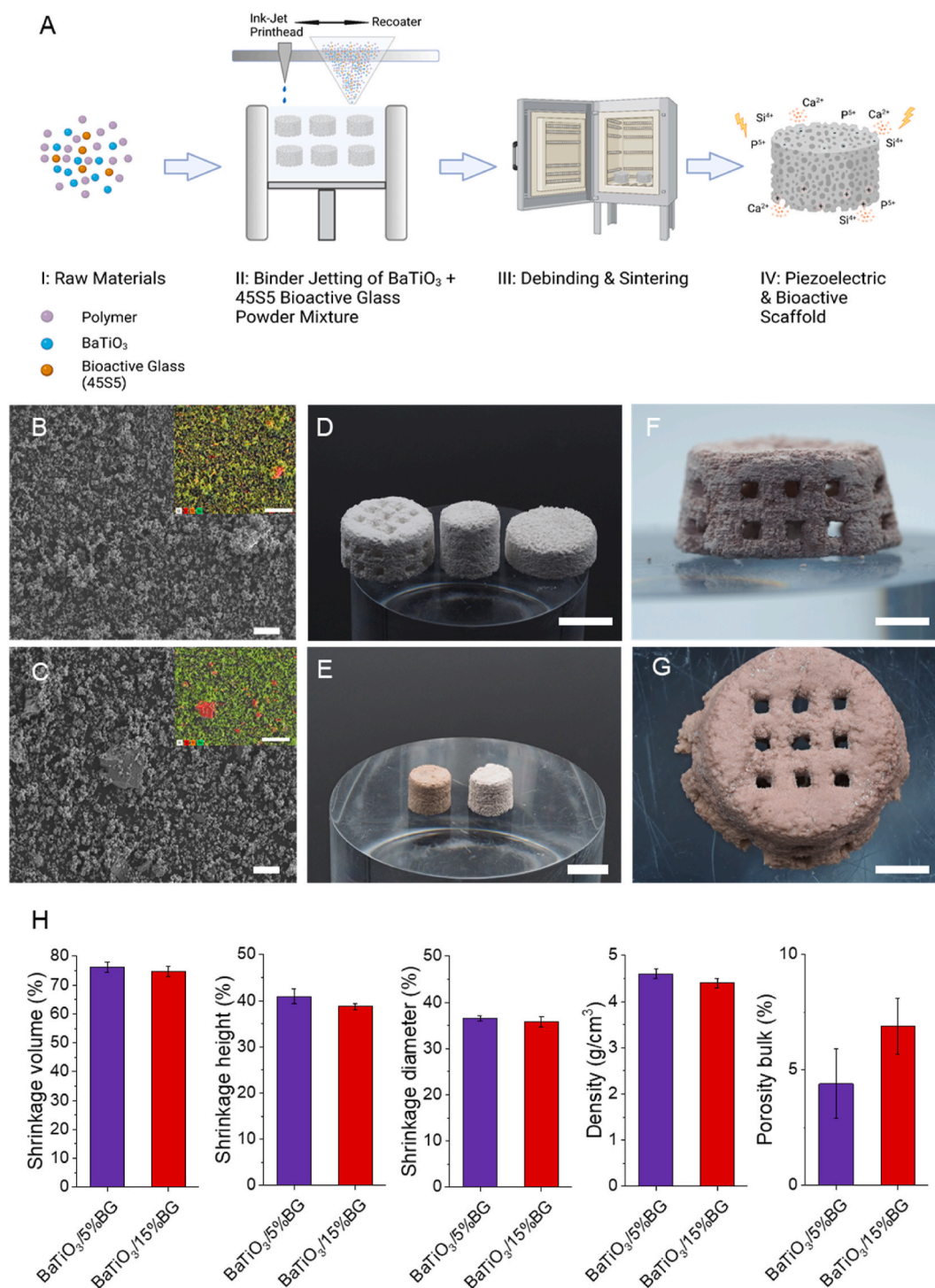


Fig. 2. Processing route for piezoelectric and bioactive BaTiO₃/BG scaffolds and 3D-printed results. (A) Schematic illustration (B–C) SEM powder analysis of both compositions containing 5% (B) and 15% (C) BG (scale bar = 20 μm). (D) Green parts printed via Binder Jetting based on the BaTiO₃/5%BG composition (scale bar = 10 mm). (E) Post-processed cylindrical samples of the BaTiO₃/5%BG (left) and BaTiO₃/15%BG (right) composite (scale bar = 10 mm). (F) Front view of a BaTiO₃/5%BG scaffold and (G) top view of a BaTiO₃/15%BG scaffold (scale bar = 5 mm). (H) Morphological and physical properties of 3D-printed BaTiO₃/BG composites. Data are shown as mean ± SD (n = 5). (For interpretation of the references to colour in this figure legend, the reader is referred to the Web version of this article.)

element mappings show the distribution of the elements in colour, with silicon shown in red, as it is the primary component in the BG, and barium shown in green (corresponding spectra are shown in Figs. S2 and S3). The powder blend prepared in this way was deposited in homogeneous layers by the 3D printer, and scaffolds were successfully produced using a binder jetting process. In the binder jetting process, the polymer

component of the powder blend is dissolved by a solvent applied based on the sliced CAD file, and the ceramic particles are firmly integrated into the polymer matrix during evaporation. Fig. 2,D shows exemplary green parts of the BaTiO₃/5%BG composited fabricated via binder jetting. We produced dense solid cylinders and interconnected porous scaffolds with a pore size of about 1 mm. After printing, it was necessary

to thermally post-process and sinter the fabricated scaffolds (Fig. 1, A III) to obtain a ceramic-crystallised glass composite. However, thermal post-treatment is critical, as the starting materials show very different sintering behaviour. BaTiO₃ conventionally sinters in a temperature range around 1300 °C [71,72], while BG (45S5) already passes two glass transition temperatures (T_{g1}, T_{g2}) at 550 °C and 850 °C and two melting temperatures at 1190 °C and 1230 °C [61,73]. Fig. 1, E shows two printed and thermally post-treated cylindrical samples of the BaTiO₃/5%BG composite on the left and the BaTiO₃/15%BG composite on the right. Both samples show a very similar appearance, with only slight differences in terms of shrinkage and a slight colour difference (Fig. 2, H). Notably, the samples of the BaTiO₃/15% BG group could not be sintered at 1320 °C due to the high content of BG and were therefore, sintered just below the first melting temperature of 45S5 BG at 1150 °C. The macroporous scaffolds were also successfully sintered and are shown in Fig. 2, F (BaTiO₃/5%BG) and G (BaTiO₃/15%BG). Noticeably,

the scaffolds are not completely accurate in shape after sintering and are expanding at the base. Since the glass transition temperatures were exceeded during sintering, which is associated with a strong reduction in the viscosity of the BG, as well as the melting point of the BG for the BaTiO₃/5%BG, the microstructure is strongly influenced by viscous flow [61,74]. The scaffolds are largely able to compensate for this, but presumably do not remain accurate in shape as a result. In this context, BG also acts as a sintering aid, allowing the sintering process to occur earlier at lower temperatures and providing greater compaction. However, the pores of the scaffolds remain free and interconnected, which is essential in terms of osteo-conduction and vascularisation [75].

4. Microstructure

The microstructural composition of ceramic-crystallised glass composites substantially influences the mechanical, dielectric and bioactive

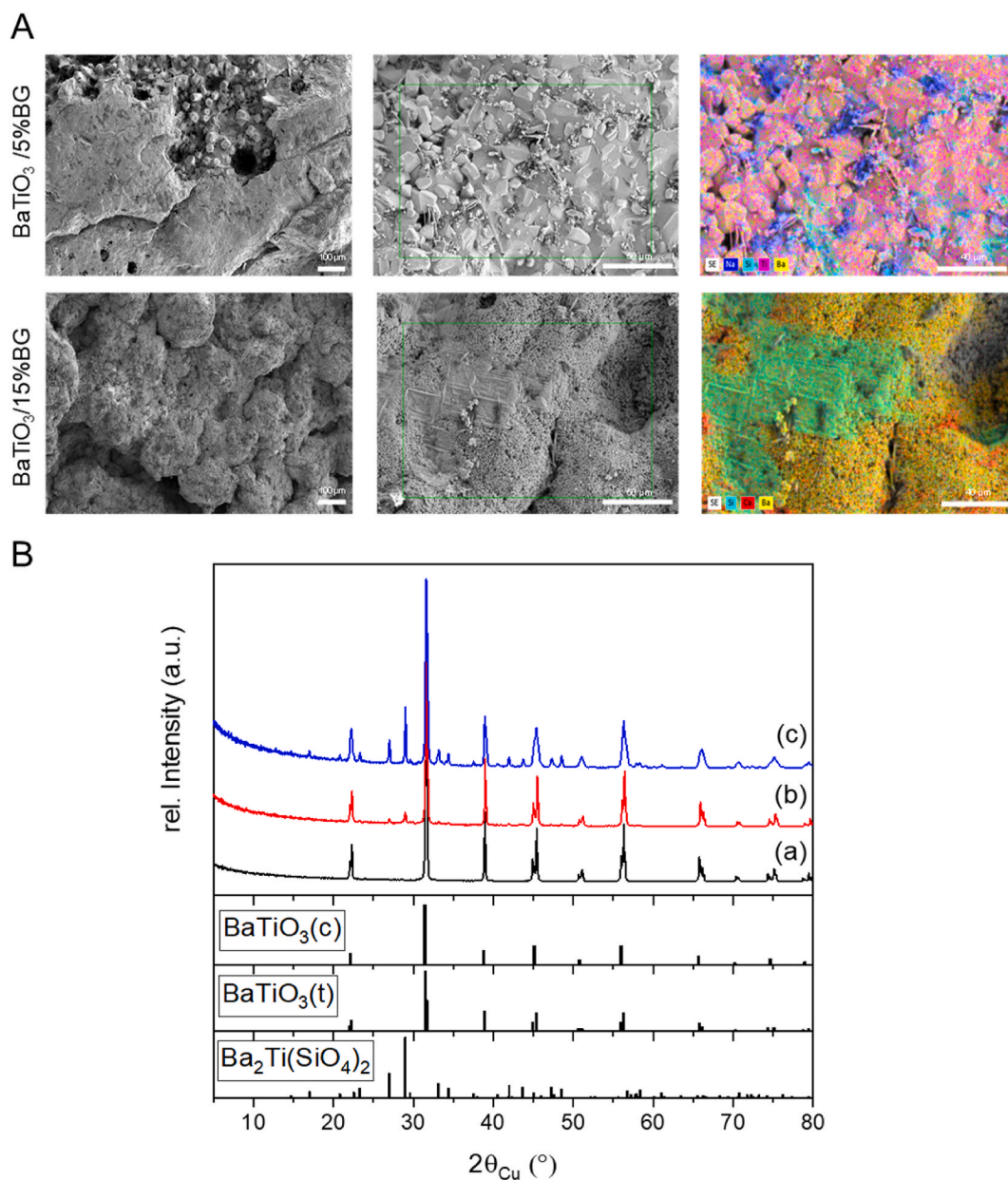


Fig. 3. Microstructural properties of thermal post-processed BaTiO₃/BG composites. (A) Representative SEM images with coupled EDS element mappings. (B) Powder X-ray diffraction pattern of utilised untreated BaTiO₃ (a), BaTiO₃/5%BG (sintered at 1320 °C; b) and BaTiO₃/15%BG (sintered at 1150 °C; c), respectively, and reference Bragg peak positions of identified main phases (cubic BaTiO₃ ICDD pdf 01-089-2475, tetragonal BaTiO₃ ICDD pdf 01-074-7965, Ba₂Ti(SiO₄)₂ 05-00-0075).

properties and is significantly affected by the necessary thermal post-treatment. Fig. 3, A shows SEM images of both composites after the respective thermal post-treatment. Both composites offer a highly compacted surface, corresponding to the porosity shown in Fig. 1, H. Only the BaTiO₃/15% BG composite sintered at 1150 °C still shows intergranular porosity and indicates that the sintering process of the BaTiO₃ is not finished. Nevertheless, with 6.9%, the bulk porosity is low, and the microstructure is largely densified. From the literature, it is known that 45S5 BG already undergoes rapid densification from the first T_{g1} (550 °C) due to the reduction of the viscosity of the glass and the onset of viscous flow. This process continues until about 600 °C when glass-in-glass separation and crystallisation processes are initiated and prevent further densification. From T_{g2} onwards, the remaining amorphous phases reach a viscosity low enough again to allow viscous flow or even liquid phase sintering, thus causing further densification of the BG and the composite [61,74]. We assume that the densification process of the BG plays a decisive role in the sintering process of the composite, especially for the higher BG loading of 15%. The intergranular pores that the BaTiO₃/15% BG composite still showed, are no longer present in the BaTiO₃/5% BG composite sintered at 1320 °C. Here, the sintering process of the BaTiO₃ particles seems to be completed. The EDS maps show portions of BG, especially Si, Na and Ca, on the surface of both composites (corresponding spectra are shown in Figs. S4 and S5). In both composites, the BG particles present in the starting material (Fig. 2 B, C) have lost their shape, which supports the assumption of viscous flow of the BG within the composite. However, the premises described in the literature refer to the sintering of pure 45S5 BG and already define dependencies on factors such as particle size, heating rates and holding times. These also apply to the composites presented here, including the presence of BaTiO₃ as a ceramic phase which interacts with the BG, e.g. through the exchange of second-order ions, significantly influencing the sintering process and the degree of crystallisation of the resulting ceramic-crystallised glass composite.

Powder X-ray diffraction has been applied to gain information about crystal phase and their potential change within the sample. For BaTiO₃, two crystalline polymorphs of cubic and tetragonal symmetry can be identified. The tetragonal phase, typically characterised by a sharp double peak at 45° 2theta, is the phase of interest for achieving desired ferroelectric and piezoelectric properties [76,77]. Obtained diffraction data of processed and sintered BaTiO₃/BG composite samples and pure BaTiO₃ are summarised in Fig. 3, B. Supporting information regarding the raw materials and the Miller indices and interplanar spacing of the major identified phases in the final composites can be found in Fig. S7 and Tables 1–3 of the supplementary information file. BaTiO₃ can still be identified from both datasets independent of the amount of BG added and treatment temperature. Notable additional phases were identified, where Ba₂TiSi₂O₈ (Fresnoite) is the most prominent one. This glass-ceramic phase which exhibits piezoelectric properties, is formed to a greater extent in BaTiO₃/BG15% compared to BaTiO₃/BG5% but shows no ferroelectric properties and cannot be polarised by an external electric field [78]. Besides, some low-intensity peaks remain unexplained in the BaTiO₃/BG15% diffraction pattern if BaTiO₃ and Ba₂TiSi₂O₈ are considered. These Bragg peaks (Fig. S6) can finally be assigned to the presence of CaTiO₃ and Na₆Ca₃Si₆O₁₈ (Combeite). As well as for Ba₂TiSi₂O₈, the presence of CaTiO₃ can be explained by the reaction of BaTiO₃ with BG, whereas Na₆Ca₃Si₆O₁₈ might result from the crystallisation of the latter. This clearly illustrated that BG undergoes structural changes from the amorphous to the crystalline state if it was treated at high temperatures. In particular, temperatures above T_{g2} (850 °C) induce the formation of crystalline sodium-calcium-silicate phases and lead to high densification of the matrix [73,79]. Recently, pseudo-piezoelectric properties for CaTiO₃ were described as well as the application as possible bone substitute material or implant coating [80–82].

4.1. Mechanical properties

We performed compression tests to assess the mechanical properties of the fabricated composites. The stress-strain curves for both ceramic-crystallised glass composites are presented in Fig. 4A and B. The curves for both composites show a similar shape but differ with respect to the time of fracture. The BaTiO₃/5%BG fails significantly earlier at lower compressive strength than the BaTiO₃/15%BG composite (Fig. 4, C). In fact, the BaTiO₃/5%BG composite exhibited an average compressive strength of 23.8 ± 4.8 MPa, and the composite with a higher BG content of 15% reached a compressive strength of 56.4 ± 7.6 MPa. The Young's moduli of both composites are very comparable, with 7.7 ± 0.9 MPa and 8.8 ± 0.5 MPa for the BaTiO₃/5%BG and the BaTiO₃/15%BG composites, respectively (Fig. 4, D). It is known that bioactive glasses can be used to enhance the mechanical properties of bioceramics such as HA and beta-TCP. Goller et al. achieved an average compressive strength of 83 MPa with a content of 5–10 wt% 45S5 in a BG/HA composite sintered between 1200 and 1300 °C [83]. Adding 5 wt% more BG to the composite increased the compressive strength of about 20 MPa, but this was dependent on the sintering temperature and could only be demonstrated for 1200 °C. For 1300 °C sintered samples, an opposite effect occurred as decomposition of the HA occurred, and unwanted reactions between the HA and the BG arose [83,84]. Similar results can be seen in the composites shown here. Increased BG content and sintering at lower temperatures increase compressive strength to 30 MPa. The higher proportion of BG in the BaTiO₃/BG15% composite and the use of lower sintering temperatures which lead to significantly more crystalline phases, appears to be the reason for the increase in compressive strength. Saeidi et al. showed comparable results for freeze-casted BaTiO₃/BG composites with 10 and 25 wt% BG loading, where the compressive strength increased similarly with the BG content [50]. Due to the very high porosity of 77%, Saeidi et al. achieved a compressive strength of 16 MPa with the BaTiO₃/BG composite with 25 wt% BG content. Shokrollahi et al. fabricated freeze-casted BaTiO₃/Akermanite (Ca₂MgSi₂O₇) scaffolds with comparable compressive strength values around 20 MPa without observing a considerable reinforcement of the composites due to an increase in the akermanite content [85]. The mechanical properties presented by us are in a similar range to those presented by other groups working with BaTiO₃-composites and in a range that is very similar to cancellous bone, making the scaffolds appealing for use in BTE, at least from a mechanical point of view. Compared to our first scaffold generation based on BaTiO₃/HA, we significantly increased the mechanical values by using BG instead of HA as a partner for BaTiO₃ [40].

4.2. Piezoelectricity

We assessed the piezoelectric properties by using the Berlincourt method exposing the polarised scaffolds to a cyclic load and measured the piezoelectric constant d₃₃ and the capacitance of the scaffolds (Fig. 5A and B). The BaTiO₃/5%BG composites exhibited an average piezoelectric constant d₃₃ of 21.2 ± 3.1 pC/N and a capacitance of 5.0 ± 0.5 pF, whereas the BaTiO₃/15%BG composites exhibited a d₃₃ of 1.2 ± 0.6 pC/N and a capacitance of 3.8 ± 0.6 pF. As expected, the increase in the BG content leads to a significant reduction of the ferroelectric and piezoelectric properties of the composite [37,50,85]. Saeidi et al. have also shown piezoelectric properties of similar magnitude for BaTiO₃/BG composites and found a decrease in the charge constant d₃₃ with an increase in BG content. Nevertheless, they were able to measure a d₃₃ of 24 pC/N up to a BG load of 25 wt% [50]. Shokrollahi et al. reported d₃₃ values in the range of 0.5–4 pC/N for BaTiO₃-akermanite composites, likewise decreasing with the increase of the non-piezoelectric phase fraction. Even small amounts of non-piezoelectric phase significantly change the microstructure of the BaTiO₃ composites, causing a pronounced degradation of the piezoelectric properties compared to pure BaTiO₃ ceramics [85]. One reason for this is the change in the

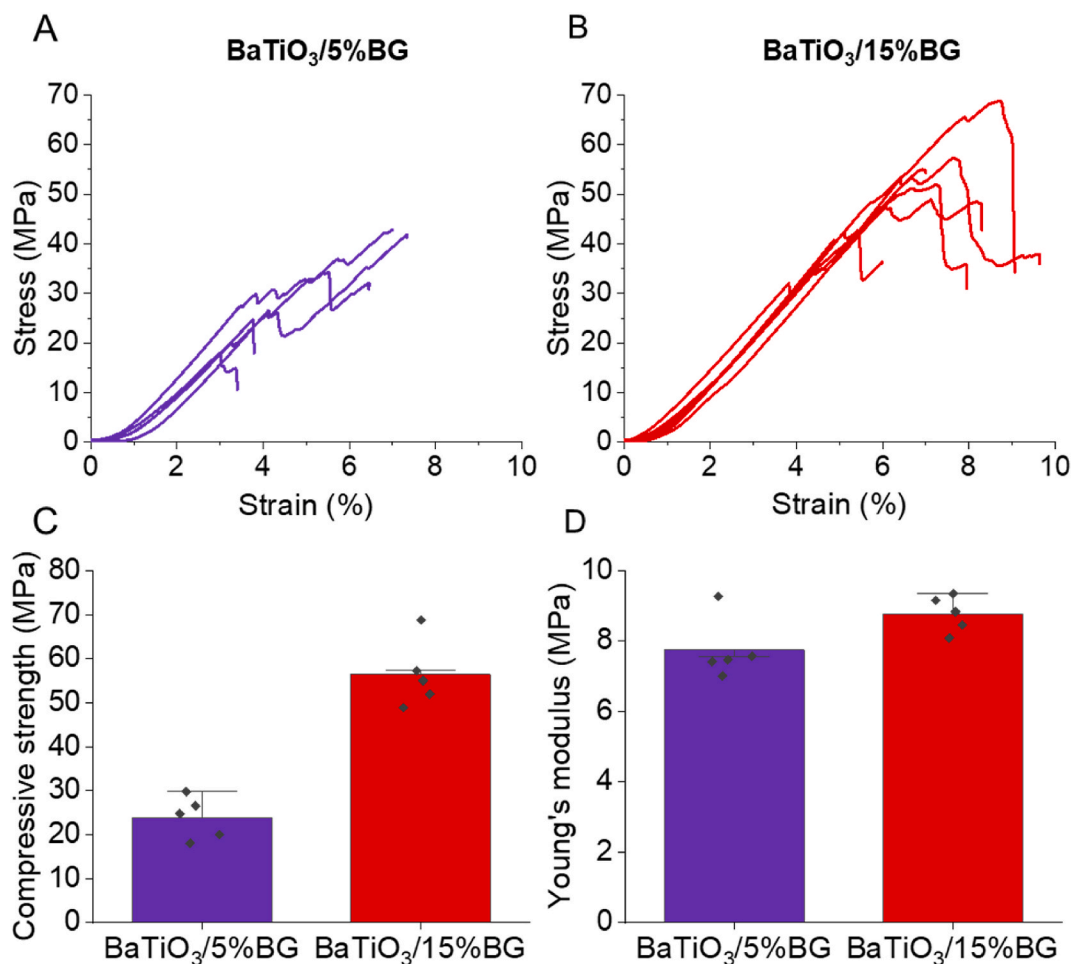


Fig. 4. Mechanical properties of 3D-printed BaTiO₃/BG composites. (A-B) Qualitative stress-strain diagrams from compression tests of BaTiO₃/5%BG (A) and BaTiO₃/15%BG (B). (C-D) Compressive strength and elastic modulus of 3D-printed BaTiO₃/5%BG (C) and BaTiO₃/15%BG (D). Data are shown as mean \pm SD (n = 5).

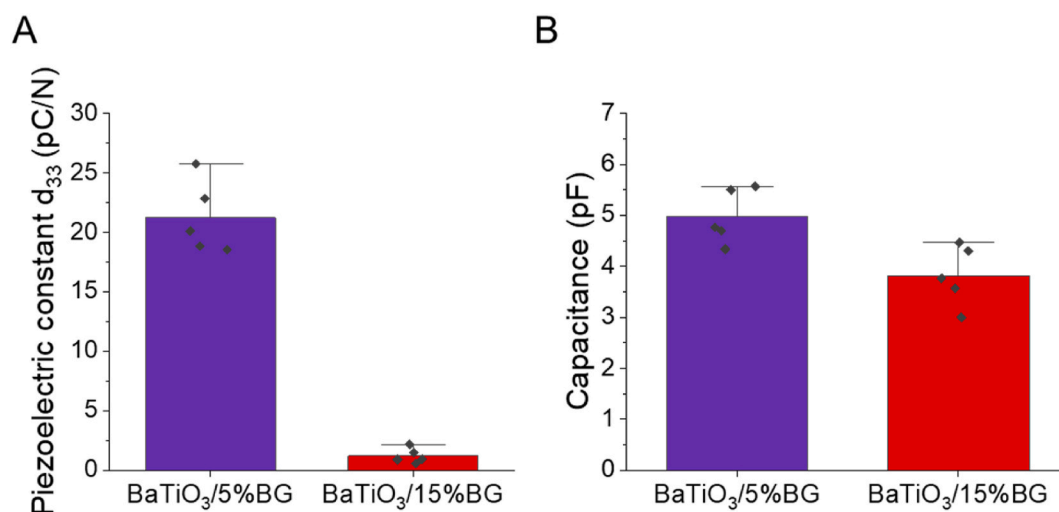


Fig. 5. Piezoelectric properties of 3D-printed BaTiO₃/BG composites. (A) Piezoelectric constant d₃₃, (B) Capacitance. Data are shown as mean \pm SD (n = 5).

composition of the material and the formation of a ceramic-crystallised glass composite. For instance, the XRD in Fig. 2, B shows the formation of different silicate phases due to the high temperature during the sintering process. The barium-titanium silicates formed, among other things, are potentially piezoelectric but not ferroelectric. This means that their dipoles do not align in the polarisation process, so they only

contribute to directional piezoelectricity to a limited extent [78]. In addition, especially for the higher loaded BaTiO₃/BG15% composite, the tetragonal crystal structure which is necessary for the piezoelectric properties of BaTiO₃, seems to degrade, which is evident from the lack of a characteristic double peak at 2 θ 45° [76]. Furthermore, due to the material inhomogeneity (pores) and the different resulting

permittivities, a uniform polarisation field is not established in the scaffolds, which can lead to an inhomogeneous remanent polarisation and thus, low piezoelectricity [86]. Overall, the results are in a range in the order of magnitude of natural bone tissue or even higher, making the scaffolds suitable candidates in a bone mimicking tissue engineering approach [87,88]. Tang et al. presented very promising results with a

composite of BaTiO₃/HA with a d₃₃ of around 2.7 pC/N, which showed significantly increased alkaline phosphatase (ALP) activity compared to pure BaTiO₃ and HA after 7 days of dynamic loading [37].

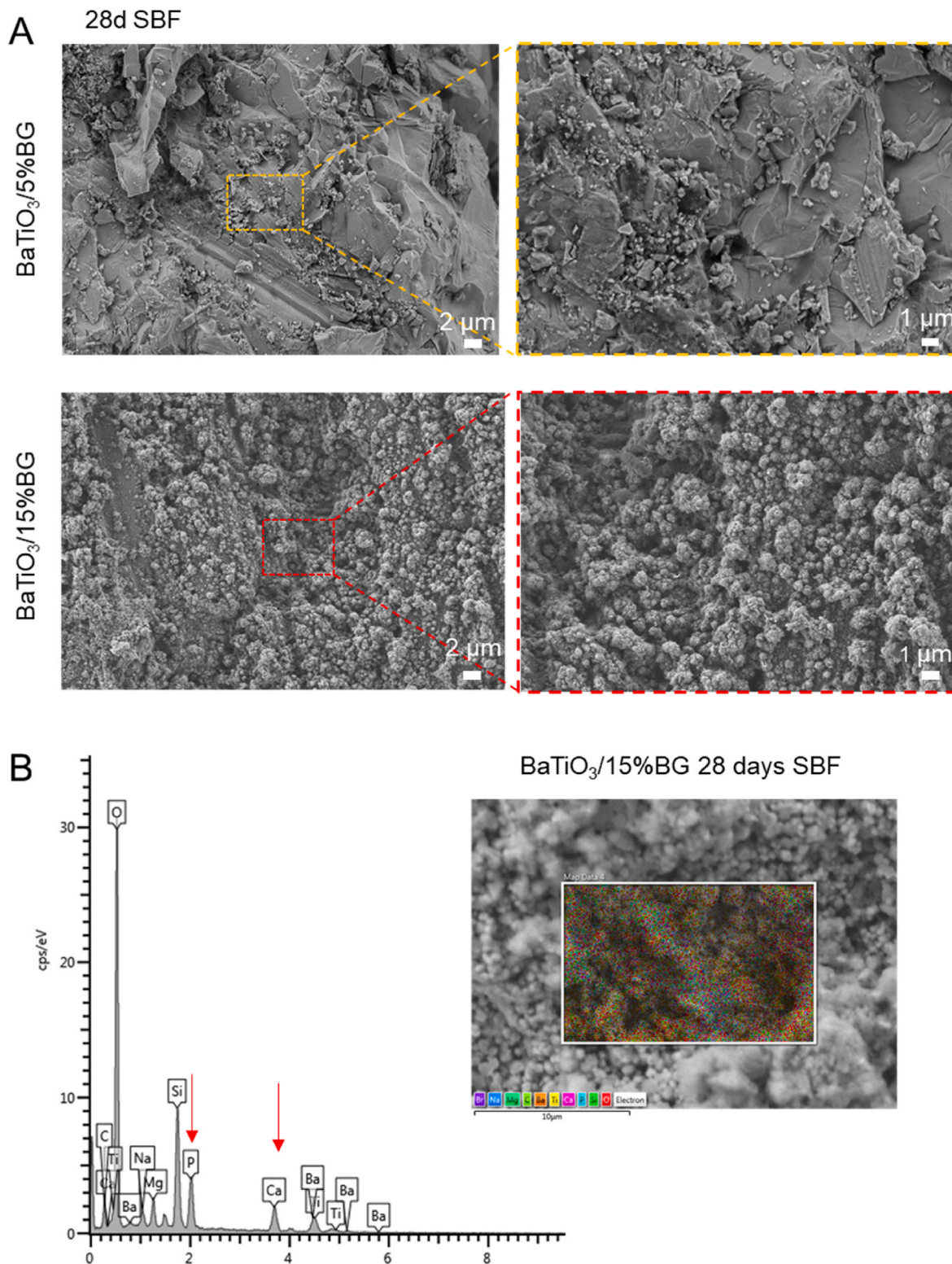


Fig. 6. Bioactivity assessment of BaTiO₃/BG composites. (A) SEM images of BaTiO₃/BG composites after 28 days of immersion in SBF showing cauliflower-like apatite formation on the surface of the BaTiO₃/15%BG composite. (B) EDS spectra on the surface of the BaTiO₃/15%BG composite.

4.3. Bioactivity

Having established the fabrication route for BaTiO₃/BG composites, and after characterisation of the major physical properties of the scaffolds, we became interested in the bioactive potential of the scaffolds. To investigate bioactivity, we incubated scaffolds of both composites for 28 days in SBF and characterised their ability to form an HCA layer [65]. An apparent change in the surface morphology became visible in the BaTiO₃/15%BG composite, where a cauliflower-like morphology developed after 28 d, indicating calcium phosphate species on the surface (Fig. 6, A) [55,89]. The BaTiO₃/5% BG scaffolds however, did not display this behaviour. On the surface of the BaTiO₃/5%BG scaffolds, particles resembling calcium phosphates are sporadically visible. The prominent formation of the characteristic cauliflower-like morphology is presumably attributed to the increased BG load and the lower sintering temperature. The EDS analysis confirms the presence of Ca and P on the surface, in addition to the prominent peaks for O, Si and Ba (Fig. 6, B).

We performed FTIR spectroscopy to assess further the formation of calcium phosphates on the surface of the scaffolds (Fig. 7). The spectra were recorded after 0 d, 7 d, 14 d, 21 d and 28 d of immersion in SBF. The BaTiO₃/15%BG composite shows more explicit indications of the formation of HCA in the spectra than the BaTiO₃/5%BG composite. From about 14 days, mid-infrared vibrations associated with PO₄³⁻ appear, represented by a bending vibration around 500 cm⁻¹ wavelength and an asymmetric stretch vibration at about 1000 cm⁻¹ [90,91]. However, the characteristic PO₄³⁻ vibrations at 560 cm⁻¹ and 604 cm⁻¹ were not detected in either composite even after 28 days in SBF [91]. A further indication of the formation of an HCA layer is the distinct detection of asymmetric CO₃²⁻ bend vibrations which increase considerably within the 28 days in SBF for the BaTiO₃/15%BG composite [91, 92]. The lower BG-loaded BaTiO₃/5%BG composite shows a reduced bioactive potential compared to the BaTiO₃/15%BG composite. The PO₄³⁻ bending vibrations at 500 cm⁻¹ are only visible to a lesser extent, and the asymmetric stretch vibrations at 1000 cm⁻¹ are absent. The CO₃²⁻ bend vibration is likewise reduced compared to the BaTiO₃/15% BG composite. The results support the insights gained from the SEM. Both composites show bioactive potential, albeit limited according to the BG content.

4.4. Cytocompatibility

An essential requirement for biomaterials is to be non-toxic and to

promote cell growth. We have, therefore, intensively investigated cytocompatibility and cell-material interaction for the 3D-printed BaTiO₃/BG composites and benchmarked them against our previous piezoelectric composite of BaTiO₃/HA [40]. For this purpose, we cultured scaffolds with MC3T3-E1 pre-osteoblasts for a period of 7 d. The results are shown in Fig. 8. After 7 d in cell culture, high growth of cells up to confluence is visible for BaTiO₃/5%BG composition, similar to the TCPS positive control (Fig. 8, A). On the BaTiO₃/HA composite, the cell layer is not as dense, and the BaTiO₃/15%BG composite shows signs of cytotoxicity due to a barely pronounced cell layer and a round cytoskeleton of the cells. The image-based quantification (Fig. 8, B) of the cell number confirms this. It reveals a significantly increased cell number of the BaTiO₃/5%BG composite compared to the BaTiO₃/HA composite of the first generation. The number of cells growing on the BaTiO₃/5%BG composite was similar to that on the TCPS pos. Control, with no significant differences. As an indicator for cell death, we used an LDH assay and quantified the extracellular LDH level (Fig. 8, C). The LDH level was significantly increased on BaTiO₃/15%BG samples, again indicating the cytotoxicity of the composition. We hypothesise that the cytotoxic effect of the BaTiO₃/15%BG composite is due to a strong burst release of hydroxide ions (OH⁻) from the ceramic-crystallised glass matrix, raising the pH value to a cytotoxic range. A measurement of the pH in the cell cultures showed a significant increase for the BaTiO₃/15BG composites compared to the scaffolds (Fig. 8, E). Such behaviour is known for BG scaffolds and can be countered with the preconditioning of the scaffolds. Therefore, it does not necessarily exclude the applicability of the higher-loaded composite as a potential biomaterial [93]. To assess the proliferation of the cells, we determined the relative DNA content using a PicoGreen QuantiT dsDNA assay. This corresponds with the image analysis and confirms a significantly higher dsDNA content on the BaTiO₃/5%BG scaffolds compared to the BaTiO₃/HA scaffolds, indicating a substantially enhanced proliferation of MC3T3 cells on the ceramic-crystallised glass composite. The SEM Image analysis (Fig. 8, F) of cells grown on BaTiO₃/5% BG, after 7 days of incubation, indicates a good cell-material and cell-cell interaction (F2, F3) with filopodia visible on the material granules from printing. The cells grow on the material, and its roughness originates from 3D printing (F3). Moreover, the cells grow into the micropores (F1) and partially bridge them, forming a cell layer on top (F4). A 3D render (Fig. 8, G) of the cell layer from confocal microscopy confirms the density of the layer and shows how much the cells can bridge the microporosity. To study the interaction of the cells with the material and the cell layer in more detail, we subsequently used two-photon microscopy (Fig. 8, H). The

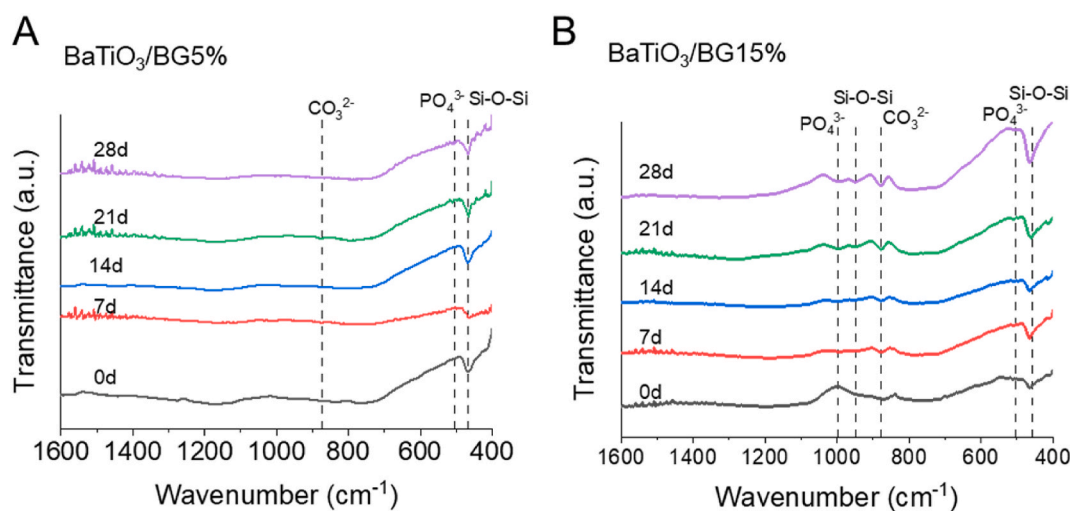
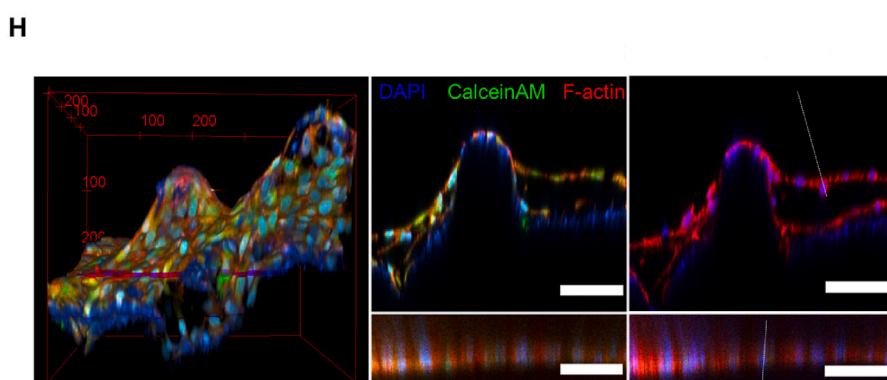
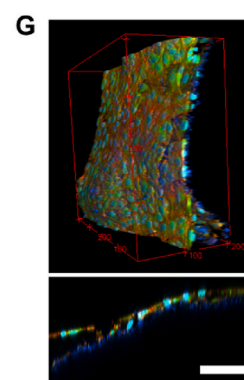
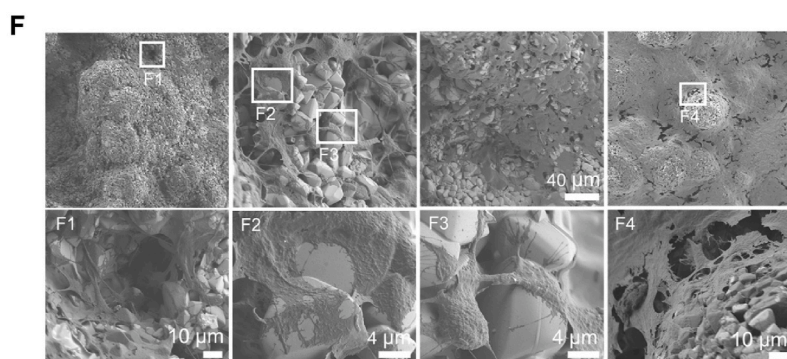
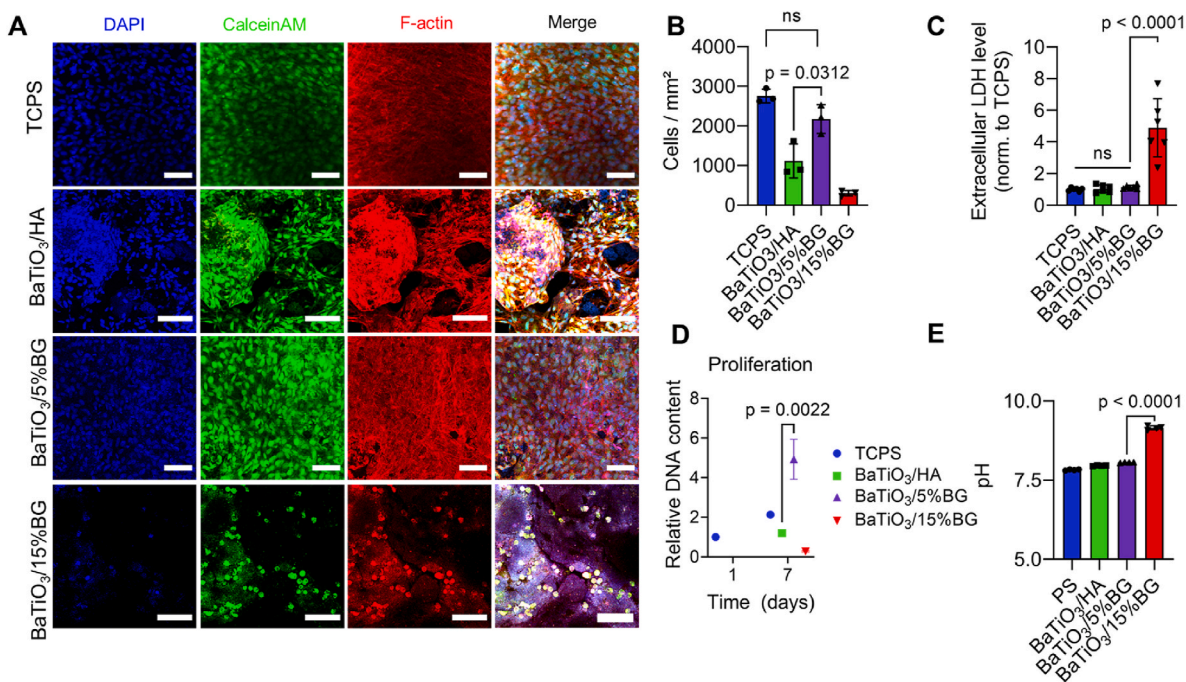


Fig. 7. FTIR of 3D-printed BaTiO₃/BG-composite scaffolds after incubation in SBF. A) FTIR spectrum for BaTiO₃/5%BG over 28d in SBF with minor PO₄³⁻ bending vibrations and CO₃²⁻ bending vibrations. B) FTIR spectrum for BaTiO₃/15%BG with more pronounced bending vibrations for PO₄³⁻ and CO₃²⁻ compared to the 5%BG composite and an additional asymmetric stretch vibration at 1000 cm⁻¹ which can also be assigned to PO₄³⁻.



(caption on next page)

Fig. 8. *In-vitro* cytocompatibility assessment of MC3T3-E1 cells on BaTiO₃/BG and first-generation BaTiO₃/HA composites. (A) Maximum intensity z-projections of DAPI (nuclei), Calcein-AM (live cells), and Rhodamine-Phalloidin (F-Actin) stained cells after seven days of incubation. **(B)** Number of cells/mm grown on the different materials, quantified via image analysis (n = 6 for BaTiO₃/HA or BaTiO₃/BG samples, n = 3 for TCPS). Data are shown as mean ± SD. Statistical analysis between groups was performed using an unpaired two-tailed Students t-test. All data were subjected to tests for normality prior to applying students t-test. **(C)** Quantification of extracellular LDH level as an indicator for cell death (n = 6). Data are shown as mean ± SD. Statistical analysis between groups was performed using an one-way ANOVA test. **(D)** The relative DNA content of samples with cells grown for seven days was quantified using PicoGreen QuantiT dsDNA assay as an indicator for cell proliferation (n = 6). Data are shown as mean ± SD statistical analysis between groups was performed using a Mann-Whitney test. **(E)** pH of the medium after 24h of cell culture (n = 6). Data are shown as mean ± SD. Statistical analysis was performed using one-way ANOVA analysis. **(F)** SEM Image analysis of cells grown on BaTiO₃/5% BG, after 7 days of incubation. 3D-render image of such cell-layer grown on BaTiO₃/5%BG for 7 days of incubation. Bottom: z-y cross-section. Scale bar = 100 μm. **(H)** Detailed image of cells grown on BaTiO₃/BG analysed via two-photon microscopy imaging, including an evaluation of the fluorescence intensity of TCPS and BaTiO₃/5%BG. Scale bars: 100 μm.

cells on the BaTiO₃/5% BG grow directly on the surface and form a levitating cell layer where the cells bridge microporosities (H'). Such a double-layered cell film explains why the relative DNA content increased compared to the TCPS pos. Control which only shows a monolayer (H''). This shows the potential of the BaTiO₃/BG composite and the 3D printing approach to specifically influence cell growth on and into the scaffolds by hierarchically built structures with designed macro and microporosity. Saeidi et al. also demonstrated a high cytocompatibility of freeze-cast BaTiO₃/BG composites of up to 98% using human mesenchymal stem cells (hMSCs) [50]. In contrast to our data, the cytocompatibility could be significantly increased with the increase in the BG fraction. The authors do not describe any signs of adverse shifts in pH due to ion release. However, they washed the scaffolds three times with PBS and presumably preconditioned them. Overall, the *in vitro* results show that especially the BaTiO₃/5%BG composite, although with limited performance in the SBF test, is an excellent candidate as a material for BTE. It is also the material combination with a higher piezoelectric charge constant d_{33} , which makes it an ideal choice for use in the combined approach as a responsive piezoelectric and bioactive material. However, other material combinations, especially in the range between 5 wt% and 15 wt% BG loading, should be considered in future studies. Finding a sweet spot that allows a better balance between piezoelectric properties, biomechanics, and bioactivity might be possible in this range. A load of 15 wt% BG should not be exceeded, as it would sacrifice the piezoelectric properties of the composite and, therefore, the possibility of further stimulating cells electrically.

5. Conclusion

In conclusion, we demonstrate the fabrication of piezoelectric and bioactive BaTiO₃/BG composite scaffolds by binder jetting for use in BTE. Starting with the description of the entire process line for the fabrication of the scaffolds, we provide a comprehensive characterisation of essential physical and functional parameters which are critical in its use as a biomaterial. The study can be summarised with the following main points:

- I) We demonstrate, for the first time, the 3D printing of BaTiO₃/BG ceramic-crystallised glass composites for biomaterial application.
- II) The manufactured specimens and scaffolds are easy to handle and show the necessary compressive strength to be a suitable bone substitute material in non-load-bearing applications.
- III) The prepared BaTiO₃/BG composites show ferroelectric and piezoelectric behaviour. The generated piezoelectric charge constant d_{33} is of the same order of magnitude or higher than that of natural bone and strongly depends on the load of BG.
- IV) An increased content of BG in the composite (BaTiO₃/15%BG) combined with a lower sintering temperature results in a pronounced HCA layer formation during SBF testing. Due to a lower BG content in the BaTiO₃/5%BG ceramic-crystallised glass composite, the HCA layer formation is limited compared to an increased load of BG.
- V) The *in vitro* experiments also indicate a dependence on BG load. In particular, the scaffolds based on the BaTiO₃/5%BG composite

show great potential in the *in vitro* experiment with no signs of cytotoxicity and strong proliferation of MC3T3 cells. BaTiO₃/15%BG scaffolds showed cytotoxic behaviour due to burst ion release and an increase in pH value. However, this could be counteracted with preconditioning, but this was not investigated in this study.

- VI) We were able to identify limits for the use of BG in a piezoelectric and bioactive composite based on BaTiO₃ and outline a possible field of conflict between individual properties, in particular bioactivity and piezoelectricity (Fig. 9).

6. Limitations and outlook

The study presented here was conceptualised as the first study exploiting the potential of piezoelectric and bioactive 3D-printed scaffolds for bone applications. The main objective was to establish a 3D printing process for piezoelectric and bioactive materials and to investigate the limitations of our material and fabrication process, especially in terms of BG loading, trying to match bioactivity with piezoelectric properties, as it is known that non-piezoelectric phases actively limit the piezoelectric properties. Therefore, we focused on low and high BG loading to find the limits of our material and process. For the material and process presented here, we were able to render a field of conflict when designing piezoelectric and bioactive 3D printed scaffolds identifying a lower and upper limit of BG load for the composites developed (Fig. 9). However, we have not yet investigated BG loadings between the loadings presented here, but these offer the potential to further improve the targeted properties of the material. Nevertheless, the BG content should be kept moderate. Otherwise, the piezoelectric properties and, thus, the possibility to electrically stimulate bone cells are lost. We will perform follow-up studies to investigate compositions between 5% and 15% BG load to tailor the material further and fine-tune the material- and process properties. Furthermore, we aim to examine the potential of scaffolds for BTE in more depth and are planning dynamic cell culture studies under targeted mechanical loading and active triggering of the piezoelectric effect. In addition, the chorioallantoic membrane (CAM) assay and *in vivo* studies in small animals are planned to investigate the biocompatibility and bioactivity of the presented composites in detail. An important focus will be to explore the potential release of Ba²⁺-ions from the BaTiO₃/BG composite matrix over a prolonged period of time in cell culture or *in vivo* to investigate possible long-term toxic effects and possible inflammatory response of the tissue [94,95]. Furthermore, we anticipate significant potential in the further development of the process. We aspire to transfer the material into much more complex structures, such as triple periodic minimal surface (TPMS) designs and integrate the structural properties described by numerous authors [96–98]. Taken together, we envision combining piezoelectric and bioactive materials with modern additive manufacturing techniques to create customised biomaterials with a tailored and controllable biological response.

Credit author contributions

Christian Polley: Conceptualisation, Methodology, Investigations,

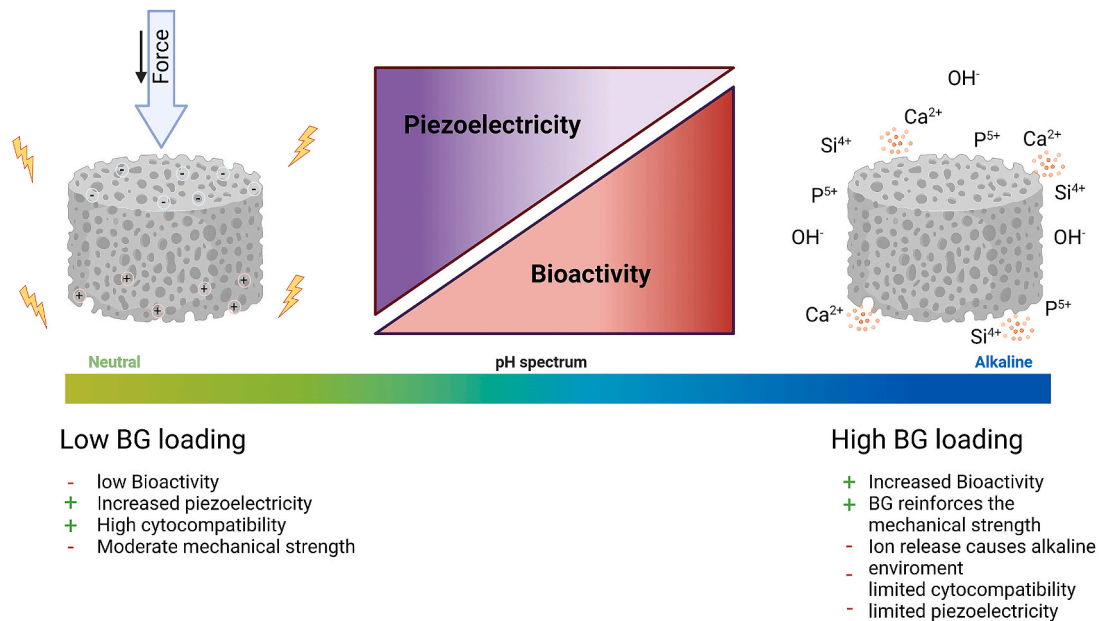


Fig. 9. Influence of BG loading on essential properties of 3D printed BaTiO₃/BG composites.

Visualisation, Formal Analysis, Writing - Original Draft, Review and Editing Thomas Distler: Investigations, Visualisation, Formal Analysis, Writing - Original Draft Caroline Scheufler: Investigations Rainer Detsch: Conceptualisation, Writing - Reviewing and Editing Henrik Lund: Investigations, Writing - Reviewing and Editing Armin Springer: Investigations, Writing - Reviewing and Editing Dominik Friederich: Investigations, Writing - Reviewing and Editing Oliver Friedrich: Investigations, Writing - Reviewing and Editing Aldo R. Boccaccini: Conceptualisation, Project Administration, Funding Acquisition, Supervision, Writing - Reviewing and Editing Hermann Seitz: Conceptualisation, Project Administration, Funding Acquisition, Supervision, Writing - Reviewing and Editing.

Ethics approval and consent to participate

It is a research manuscript and human subjects or animals were not involved. Therefore no “ethics approval and consent” is needed.

Declaration of competing interest

The authors declare that they have no known competing financial interests or personal relationships that could have appeared to influence the work reported in this paper.

Data availability

Data will be made available on request.

Acknowledgements

This research was funded by Deutsche Forschungsgemeinschaft (DFG, German Research Foundation) – SFB 1270/1,2–299150580 to Hermann Seitz and Aldo R. Boccaccini and TRR225 subproject B08/Z02 to Oliver Friedrich. We also thank the technical staff of all institutes who successfully helped with the investigations. The Graphical Abstract and Fig. 1A & Fig. 9 were created with Biorender.com.

Appendix A. Supplementary data

Supplementary data to this article can be found online at <https://doi.org/10.1016/j.mtbio.2023.100719>.

[org/10.1016/j.mtbio.2023.100719](https://doi.org/10.1016/j.mtbio.2023.100719).

References

- [1] K. Zhang, S. Wang, C. Zhou, L. Cheng, X. Gao, X. Xie, J. Sun, H. Wang, M.D. Weir, M.A. Reynolds, N. Zhang, Y. Bai, H.H.K. Xu, Advanced smart biomaterials and constructs for hard tissue engineering and regeneration, *Bone Res* 6 (2018), <https://doi.org/10.1038/s41413-018-0032-9>.
- [2] B.M. Holzapfel, J.C. Reichert, J.T. Schantz, U. Gbureck, L. Rackwitz, U. Nöth, F. Jakob, M. Rudert, J. Groll, D.W. Hutmacher, How smart do biomaterials need to be? A translational science and clinical point of view, *Adv. Drug Deliv. Rev.* 65 (2013) 581–603, <https://doi.org/10.1016/j.addr.2012.07.009>.
- [3] L.L. Hench, R.J. Splinter, W.C. Allen, T.K. Greenlee, Bonding mechanisms at the interface of ceramic prosthetic materials, *J. Biomed. Mater. Res.* 5 (1971) 117–141, <https://doi.org/10.1002/JBM.820050611>.
- [4] L.L. Hench, The story of Bioglass, *J. Mater. Sci. Mater. Med.* (2006) 967–978, <https://doi.org/10.1007/s10856-006-0432-z>.
- [5] S. Radin, G. Reilly, G. Bhargava, P.S. Leboy, P. Ducheyne, Osteogenic effects of bioactive glass on bone marrow stromal cells, *J. Biomed. Mater. Res., Part A* 73 (2005) 21–29, <https://doi.org/10.1002/jbm.a.37136>.
- [6] F. Westhauser, S. Wilkesmann, Q. Nawaz, F. Hohenbild, F. Rehder, M. Saur, J. Fellenberg, A. Moghaddam, M.S. Ali, W. Peukert, A.R. Boccaccini, Effect of manganese, zinc, and copper on the biological and osteogenic properties of mesoporous bioactive glass nanoparticles, *J. Biomed. Mater. Res., Part A* 109 (2021) 1457–1467, <https://doi.org/10.1002/jbm.a.37136>.
- [7] J. Moura, L.N. Teixeira, C. Ravagnani, O. Peitl, E.D. Zanotto, M.M. Beloti, H. Panzeri, A.L. Rosa, P.T. De Oliveira, In vitro osteogenesis on a highly bioactive glass-ceramic (Biosilicate®), *J. Biomed. Mater. Res., Part A* 82 (2007) 545–557, <https://doi.org/10.1002/jbm.a.31165>.
- [8] L. Weng, S.K. Boda, M.J. Teusink, F.D. Shuler, X. Li, J. Xie, Binary doping of strontium and copper enhancing osteogenesis and angiogenesis of bioactive glass nanofibers while suppressing osteoclast activity, *ACS Appl. Mater. Interfaces* 9 (2017) 24484–24496, <https://doi.org/10.1021/acsami.7b06521>.
- [9] A. Hoppe, N.S. Güldal, A.R. Boccaccini, A review of the biological response to ionic dissolution products from bioactive glasses and glass-ceramics, *Biomaterials* 32 (2011) 2757–2774, <https://doi.org/10.1016/j.biomaterials.2011.01.004>.
- [10] V. Miguez-Pacheco, L.L. Hench, A.R. Boccaccini, Bioactive glasses beyond bone and teeth: emerging applications in contact with soft tissues, *Acta Biomater.* 13 (2015) 1–15, <https://doi.org/10.1016/j.actbio.2014.11.004>.
- [11] L.C. Gerhardt, K.L. Widdows, M.M. Erol, C.W. Burch, J.A. Sanz-Herrera, I. Ochoa, R. Stämpfli, I.S. Roqan, S. Gabe, T. Ansari, A.R. Boccaccini, The pro-angiogenic properties of multi-functional bioactive glass composite scaffolds, *Biomaterials* 32 (2011) 4096–4108, <https://doi.org/10.1016/j.biomaterials.2011.02.032>.
- [12] G. Bühner, U. Rottensteiner, A. Hoppe, R. Detsch, D. Dafinova, T. Fey, P. Greil, C. Weis, J.P. Beier, A.R. Boccacini, R.E. Horch, A. Arkudas, Evaluation of in vivo angiogenic effects of copper doped bioactive glass scaffolds in the AV loop model, in: *Biomed. Glas., Walter de Gruyter GmbH*, 2016, pp. 111–117, <https://doi.org/10.1515/bglass-2016-0013>.
- [13] J.S. Fernandes, P. Gentile, R.A. Pires, R.L. Reis, P.V. Hatton, Multifunctional bioactive glass and glass-ceramic biomaterials with antibacterial properties for repair and regeneration of bone tissue, *Acta Biomater.* 59 (2017) 2–11, <https://doi.org/10.1016/j.actbio.2017.06.046>.

- [14] J.R. Jones, L.M. Ehrenfried, P. Saravanapavan, L.L. Hench, Controlling ion release from bioactive glass foam scaffolds with antibacterial properties, *J. Mater. Sci. Mater. Med.* (2006) 989–996, <https://doi.org/10.1007/s10856-006-0434-x>.
- [15] S. Kargozar, M. Montazerian, S. Hamzehlou, H.W. Kim, F. Baino, Mesoporous bioactive glasses: promising platforms for antibacterial strategies, *Acta Biomater.* 81 (2018) 1–19, <https://doi.org/10.1016/j.actbio.2018.09.052>.
- [16] K. Zheng, E. Torre, A. Bari, N. Taccardi, C. Cassinelli, M. Morra, S. Fiorilli, C. Vitale-Brovarone, G. Iviglia, A.R. Boccaccini, Antioxidant mesoporous Ce-doped bioactive glass nanoparticles with anti-inflammatory and pro-osteogenic activities, *Mater. Today Bio.* 5 (2020), <https://doi.org/10.1016/j.mtbio.2020.100041>.
- [17] S. Majumdar, S.K. Hira, H. Tripathi, A.S. Kumar, P.P. Manna, S.P. Singh, S. Krishnamurthy, Synthesis and characterization of barium-doped bioactive glass with potential anti-inflammatory activity, *Ceram. Int.* 47 (2021) 7143–7158, <https://doi.org/10.1016/j.ceramint.2020.11.068>.
- [18] F.N. Barrak, S. Li, A.A. Mohammed, C. Myant, J.R. Jones, Anti-inflammatory properties of S53P4 bioactive glass implant material, *J. Dent.* 127 (2022), 104296, <https://doi.org/10.1016/j.jdent.2022.104296>.
- [19] D.S. Brauer, Bioactive glasses - structure and properties, *Angew. Chem. Int. Ed.* 54 (2015) 4160–4181, <https://doi.org/10.1002/anie.201405310>.
- [20] F. Baino, E. Fiume, J. Barberi, S. Kargozar, J. Marchi, J. Massera, E. Verné, Processing methods for making porous bioactive glass-based scaffolds—a state-of-the-art review, *Int. J. Appl. Ceram. Technol.* 16 (2019) 1762–1796, <https://doi.org/10.1111/IJAC.13195>.
- [21] E. Zeimaran, S. Pourshahrestani, A. Fathi, N.A. bin A. Razak, N.A. Kadri, A. Sheikhi, F. Baino, Advances in bioactive glass-containing injectable hydrogel biomaterials for tissue regeneration, *Acta Biomater.* 136 (2021) 1–36, <https://doi.org/10.1016/j.actbio.2021.09.034>.
- [22] A.H. Rajabi, M. Jaffe, T.L. Arinze, Piezoelectric materials for tissue regeneration: a review, *Acta Biomater.* 24 (2015) 12–23, <https://doi.org/10.1016/j.actbio.2015.07.010>.
- [23] B. Tandon, J.J. Blaker, S.H. Cartmell, Piezoelectric materials as stimulatory biomedical materials and scaffolds for bone repair, *Acta Biomater.* 73 (2018) 1–20, <https://doi.org/10.1016/j.actbio.2018.04.026>.
- [24] K. Kapat, Q.T.H. Shubhra, M. Zhou, S. Leeuwenburgh, Piezoelectric nano-biomaterials for biomedicine and tissue regeneration, *Adv. Funct. Mater.* 30 (2020), <https://doi.org/10.1002/adfm.201909045>.
- [25] J. Jacob, N. More, K. Kalita, G. Kapusetti, Piezoelectric Smart Biomaterials for Bone and Cartilage Tissue Engineering, *Inflamm. Regen.* (n.d.), <https://doi.org/10.1186/s41232-018-0059-8>.
- [26] J. Curie, P. Curie, Développement par compression de l'électricité polaire dans les cristaux hémihédres à faces inclinées, *Bull. Mineral.* 3 (1880) 90–93, <https://doi.org/10.3406/BULML.1880.1564>.
- [27] E. Fukada, I. Yasuda, On the piezoelectric effect of bone, *J. Phys. Soc. Japan.* 12 (1957) 1158–1162, <https://doi.org/10.1143/JPSJ.12.1158>.
- [28] E. Fukada, I. Yasuda, Piezoelectric effects in collagen, *Jpn. J. Appl. Phys.* 3 (1964) 117–121, <https://doi.org/10.1143/JJAP.3.117>.
- [29] C. Andrew, L. Bassett, *Biologic Significance of Piezoelectricity**, 1968.
- [30] F. Sahn, A. Jakovljevic, R. Bader, R. Detsch, A. Jonitz-Heincke, Is there an influence of electrically stimulated osteoblasts on the induction of osteoclastogenesis? *Appl. Sci.* 12 (2022), <https://doi.org/10.3390/app122211840>.
- [31] T. Kreller, J. Zimmermann, U. van Rienen, A.R. Boccaccini, A. Jonitz-Heincke, R. Detsch, Alternating electric field stimulation: phenotype analysis and osteoclast activity of differentiated RAW 264.7 macrophages on hydroxyapatite-coated Ti6Al4V surfaces and their crosstalk with MC3T3-E1 pre-osteoblasts, *Biomater. Adv.* 146 (2023), <https://doi.org/10.1016/j.bioadv.2023.213285>.
- [32] D. Khare, B. Basu, A.K. Dubey, Electrical stimulation and piezoelectric biomaterials for bone tissue engineering applications, *Biomaterials* (2020) 258, <https://doi.org/10.1016/j.biomaterials.2020.120280>.
- [33] S.A.M. Tofail, D. Haverty, F. Cox, J. Erhart, P. Hána, V. Ryzhenko, Dielectric relaxation in monoclinic hydroxyapatite: observation of hydroxide ion dipoles, *Cit. J. Appl. Phys.* 105 (2009), 74701, <https://doi.org/10.1063/1.3093863>.
- [34] A.C. Ahn, A.J. Grodzinsky, Relevance of collagen piezoelectricity to "Wolff's Law": a critical review., *Med. Eng. Phys.* 31 (2009) 733–41, <https://doi.org/10.1016/j.medengphy.2009.02.006>.
- [35] J.B. Park, B.J. Kelly, G.H. Kenner, A.F. von Recum, M.F. Grether, W.W. Coffeen, Piezoelectric ceramic implants: in vivo results, *J. Biomed. Mater. Res.* 15 (1981) 103–110, <https://doi.org/10.1002/jbm.820150114>.
- [36] W. Liu, D. Yang, X. Wei, S. Guo, N. Wang, Z. Tang, Y. Lu, S. Shen, L. Shi, X. Li, Z. Guo, Fabrication of piezoelectric porous BaTiO₃ scaffold to repair large segmental bone defect in sheep, *J. Biomater. Appl.* (2020), <https://doi.org/10.1177/0885328220942906>.
- [37] Y. Tang, C. Wu, Z. Wu, L. Hu, W. Zhang, K. Zhao, Fabrication and in vitro biological properties of piezoelectric bioceramics for bone regeneration, *Sci. Rep.* 7 (2017), 43360, <https://doi.org/10.1038/srep43360>.
- [38] F.R. Baxter, I.G. Turner, C.R. Bowen, J.P. Gittings, J.B. Chaudhuri, An in vitro study of electrically active hydroxyapatite-barium titanate ceramics using Saos-2 cells, *J. Mater. Sci. Mater. Med.* 20 (2009) 1697–1708, <https://doi.org/10.1007/s10856-009-3734-0>.
- [39] K.K. Poon, M.C. Wurm, D.M. Evans, M. Einarsrud, R. Lutz, J. Glaum, Biocompatibility of (Ba,Ca)(Zr,Ti)O₃ piezoelectric ceramics for bone replacement materials, *J. Biomed. Mater. Res. Part B Appl. Biomater.* 108 (2020) 1295–1303, <https://doi.org/10.1002/jbm.b.34477>.
- [40] C. Polley, T. Distler, R. Detsch, H. Lund, A. Springer, A.R. Boccaccini, H. Seitz, 3D printing of piezoelectric barium titanate-hydroxyapatite scaffolds with interconnected porosity for bone tissue engineering, *Materials* 13 (2020) 1773, <https://doi.org/10.3390/ma13071773>.
- [41] K.K. Poon, S. Schafföner, M.A. Einarsrud, J. Glaum, Barium titanate-based bilayer functional coatings on Ti alloy biomedical implants, *J. Eur. Ceram. Soc.* 41 (2021) 2918–2922, <https://doi.org/10.1016/j.jeurceramsoc.2020.12.023>.
- [42] A. Riaz, C. Polley, H. Lund, A. Springer, H. Seitz, A novel approach to fabricate load-bearing Ti6Al4V-Barium titanate piezoelectric bone scaffolds by coupling electron beam melting and field-assisted sintering, *Mater. Des.* 225 (2023), 111428, <https://doi.org/10.1016/j.matdes.2022.111428>.
- [43] P. Vaněk, Z. Kolská, T. Luxbacher, J.A.L. García, M. Lehocký, M. Vandrovová, L. Bačáková, J. Petzelt, Electrical activity of ferroelectric biomaterials and its effects on the adhesion, growth and enzymatic activity of human osteoblast-like cells, *J. Phys. D Appl. Phys.* 49 (2016), 175403, <https://doi.org/10.1088/0022-3727/49/17/175403>.
- [44] V. Marchesano, O. Gennari, L. Mecozzi, S. Grilli, P. Ferraro, Effects of lithium niobate polarization on cell adhesion and morphology, *ACS Appl. Mater. Interfaces* 7 (2015) 18113–18119, https://doi.org/10.1021/ACSAMI.5B05340/ASSET/IMAGES/LARGE/AM-2015-05340A_0012.
- [45] P.M. Vilarinho, N. Barroca, S. Zlotnik, P. Félix, M.H. Fernandes, Are lithium niobate (LiNbO₃) and lithium tantalate (LiTaO₃) ferroelectric bioactive? *Mater. Sci. Eng., C* 39 (2014) 395–402, <https://doi.org/10.1016/j.msec.2014.03.026>.
- [46] Q. Wang, Q. Chen, J. Zhu, C. Huang, B.W. Darvell, Z. Chen, Effects of pore shape and porosity on the properties of porous LKNK ceramics as bone substitute, *Mater. Chem. Phys.* 109 (2008) 488–491, <https://doi.org/10.1016/j.matchemphys.2007.12.022>.
- [47] A.K. Dubey, R. Kinoshita, K.I. Kakimoto, Piezoelectric sodium potassium niobate mediated improved polarization and in vitro bioactivity of hydroxyapatite, *RSC Adv.* 5 (2015) 19638–19646, <https://doi.org/10.1039/C5RA00771B>.
- [48] N.H. Gaukås, Q.S. Huynh, A.A. Pratap, M.A. Einarsrud, T. Grande, R.M. D. Holsinger, J. Glaum, *In vitro* biocompatibility of piezoelectric K_{0.5}Na_{0.5}Nb_{0.3}Thin films on platinumized silicon substrates, *ACS Appl. Bio Mater.* 3 (2020) 8714–8721, <https://doi.org/10.1021/acsbio.0c01111>.
- [49] W. Chen, Z. Yu, J. Pang, P. Yu, G. Tan, C. Ning, Fabrication of biocompatible potassium sodium niobate piezoelectric ceramic as an electroactive implant, *Materials* 10 (2017) 345, <https://doi.org/10.3390/MA10040345>, 10 (2017) 345.
- [50] B. Saeidi, M.R. Derakhshandeh, M. Delshad Chermahini, A. Doostmohammadi, Novel porous barium titanate/nano-bioactive glass composite with high piezoelectric coefficient for bone regeneration applications, *J. Mater. Eng. Perform.* 29 (2020) 5420–5427, <https://doi.org/10.1007/s11665-020-05016-0>.
- [51] F. Zhao, C. Zhang, J. Liu, L. Liu, X. Cao, X. Chen, B. Lei, L. Shao, Periosteum structure/function-mimicking bioactive scaffolds with piezoelectric/chem/nano signals for critical-sized bone regeneration, *Chem. Eng. J.* 402 (2020), 126203, <https://doi.org/10.1016/j.cej.2020.126203>.
- [52] D. Goltzman, G.N. Hendy, The calcium-sensing receptor in bone-mechanistic and therapeutic insights, *Nat. Rev. Endocrinol.* 11 (2015) 298–307, <https://doi.org/10.1038/nrendo.2015.30>.
- [53] M. Martens, R. Van Audekercke, P. Delpoit, P. De Meester, J.C. Mulier, The mechanical characteristics of cancellous bone at the upper femoral region, *J. Biomech.* 16 (1983) 971–983, [https://doi.org/10.1016/0021-9290\(83\)90098-2](https://doi.org/10.1016/0021-9290(83)90098-2).
- [54] J.W. Vahey, J.L. Lewis, R. Vanderby, Elastic moduli, yield stress, and ultimate stress of cancellous bone in the canine proximal femur, *J. Biomech.* 20 (1987) 29–33, [https://doi.org/10.1016/0021-9290\(87\)90264-8](https://doi.org/10.1016/0021-9290(87)90264-8).
- [55] T. Distler, N. Fournier, A. Grünewald, C. Polley, H. Seitz, R. Detsch, A. R. Boccaccini, Polymer-bioactive glass composite filaments for 3D scaffold manufacturing by fused deposition modeling: fabrication and characterization, *Front. Bioeng. Biotechnol.* 8 (2020) 552, <https://doi.org/10.3389/fbioe.2020.00552>.
- [56] C. Polzin, S. Spath, H. Seitz, Characterization and evaluation of a PMMA-based 3D printing process, *Rapid Prototyp. J.* 19 (2013) 37–43, <https://doi.org/10.1108/13552541311292718>.
- [57] H. Takahashi, Y. Numamoto, J. Tani, K. Matsuta, J. Qiu, S. Tsurekawa, Lead-free barium titanate ceramics with large piezoelectric constant fabricated by microwave sintering, *Jpn. J. Appl. Phys., Part 2* 45 (2006), <https://doi.org/10.1143/JJAP.45.L30>.
- [58] S.M. Gaytan, M.A. Cadena, H. Karim, D. Delfin, Y. Lin, D. Espalin, E. MacDonald, R. B. Wicker, Fabrication of barium titanate by binder jetting additive manufacturing technology, *Ceram. Int.* (2015), <https://doi.org/10.1016/j.ceramint.2015.01.108>.
- [59] W. Wang, J. Sun, B. Guo, X. Chen, K.P. Ananth, J. Bai, Fabrication of piezoelectric nano-ceramics via stereolithography of low viscous and non-aqueous suspensions, *J. Eur. Ceram. Soc.* 40 (2020) 682–688, <https://doi.org/10.1016/j.jeurceramsoc.2019.10.033>.
- [60] B. Dai, X. Hu, R. Yin, W. Bai, F. Wen, J. Deng, L. Zheng, J. Du, P. Zheng, H. Qin, Piezoelectric grain-size effects of BaTiO₃ ceramics under different sintering atmospheres, *J. Mater. Sci. Mater. Electron.* 28 (2017) 7928–7934, <https://doi.org/10.1007/s10854-017-6494-5>.
- [61] A.R. Boccaccini, Q. Chen, L. Lefebvre, L. Gremillard, J. Chevalier, Sintering, crystallisation and biodegradation behaviour of Bioglass®-derived glass-ceramics, *Faraday Discuss* 136 (2007) 27–44, <https://doi.org/10.1039/b616539g>.
- [62] O. Bretcanu, X. Chatzistavrou, K. Paraskevopoulos, R. Conradt, I. Thompson, A. R. Boccaccini, Sintering and crystallisation of 45S5 Bioglass® powder, *J. Eur. Ceram. Soc.* 29 (2009) 3299–3306, <https://doi.org/10.1016/j.jeurceramsoc.2009.06.035>.
- [63] C. Polley, S. Schulze, T. Distler, R. Detsch, A.R. Boccaccini, H. Seitz, Sintering Behavior of 3D Printed Barium Titanate Composite Scaffolds for Bone Repair, 2020, <https://doi.org/10.18416/AMMM.2020.2009019>.
- [64] M. Stewart, W. Battrick, M. Cain, *Measurement Good Practice Guide No. 44 Measuring Piezoelectric D 33 Coefficients Using the Direct Method Measuring Piezoelectric D 33 Coefficients Using the Direct Method* Contents, 2001.

- [65] T. Kokubo, Bioactive Glass Ceramics: Properties and Applications, n.d.
- [66] T. Distler, C. Polley, F. Shi, D. Schneidereit, M.D. Ashton, O. Friedrich, J.F. Kolb, J. G. Hardy, R. Detsch, H. Seitz, A.R. Boccaccini, Electrically conductive and 3D-printable oxidized alginate-gelatin polypyrrole:PSS hydrogels for tissue engineering, *Adv. Healthc. Mater.* 10 (2021), <https://doi.org/10.1002/adhm.202001876>.
- [67] T. Distler, C. Polley, F. Shi, D. Schneidereit, M.D. Ashton, O. Friedrich, J.F. Kolb, J. G. Hardy, R. Detsch, H. Seitz, A.R. Boccaccini, Electrically conductive and 3D-printable oxidized alginate-gelatin polypyrrole:PSS hydrogels for tissue engineering, *Adv. Healthc. Mater.* 10 (2021), <https://doi.org/10.1002/adhm.202001876>.
- [68] M. Rizwan, M. Hamdi, W.J. Basirun, Bioglass® 45S5-based composites for bone tissue engineering and functional applications, *J. Biomed. Mater. Res., Part A* 105 (2017) 3197–3223, <https://doi.org/10.1002/jbm.a.36156>.
- [69] C. Polley, T. Distler, D. Ruffer, R. Detsch, A.R. Boccaccini, H. Seitz, 3D printing of smart materials for bone regeneration, *Trans. Addit. Manuf. Meets Med.* 1 (2019), <https://doi.org/10.18416/AMMM.2019.1909507703>.
- [70] M. Schult, E. Buckow, H. Seitz, Experimental studies on 3D printing of barium titanate ceramics for medical applications, *Curr. Dir. Biomed. Eng.* 2 (2016) 95–99, <https://doi.org/10.1515/cdbme-2016-0024>.
- [71] W. Maison, R. Kleeberg, R.B. Heimann, S. Phanichphant, Phase content, tetragonality, and crystallite size of nanoscaled barium titanate synthesized by the catechol process: effect of calcination temperature, *J. Eur. Ceram. Soc.* 23 (2003) 127–132, [https://doi.org/10.1016/S0955-2219\(02\)00071-7](https://doi.org/10.1016/S0955-2219(02)00071-7).
- [72] S.Y. Choi, S.J.L. Kang, Sintering kinetics by structural transition at grain boundaries in barium titanate, *Acta Mater.* 52 (2004) 2937–2943, <https://doi.org/10.1016/J.ACTAMAT.2004.02.039>.
- [73] D. Bellucci, V. Cannillo, A. Sola, An overview of the effects of thermal processing on bioactive glasses, *Sci. Sinter.* 42 (2010) 307–320, <https://doi.org/10.2298/SOS1003307B>.
- [74] L. Lefebvre, L. Gremillard, J. Chevalier, R. Zenati, D. Bernache-Assolant, Sintering behaviour of 45S5 bioactive glass, *Acta Biomater.* 4 (2008) 1894–1903, <https://doi.org/10.1016/j.actbio.2008.05.019>.
- [75] V. Karageorgiou, D. Kaplan, Porosity of 3D biomaterial scaffolds and osteogenesis, *Biomaterials* 26 (2005) 5474–5491, <https://doi.org/10.1016/J.BIOMATERIALS.2005.02.002>.
- [76] H.W. Lee, S. Moon, C.H. Choi, D.K. Kim, Synthesis and size control of tetragonal barium titanate nanopowders by facile solvothermal method, *J. Am. Ceram. Soc.* 95 (2012) 2429–2434, <https://doi.org/10.1111/J.1551-2916.2012.05085.X>.
- [77] C. Chen, H. Hao, T. Wang, J. Cheng, Z. Luo, L. Zhang, M. Cao, Z. Yao, H. Liu, Nano-BaTiO₃ phase transition behavior in coated BaTiO₃-based dielectric ceramics, *Ceram. Int.* 45 (2019) 7166–7172, <https://doi.org/10.1016/J.CERAMINT.2018.12.223>.
- [78] W. Wisniewski, K. Thieme, C. Rüssel, Fresnoite glass-ceramics – a review, *Prog. Mater. Sci.* 98 (2018) 68–107, <https://doi.org/10.1016/j.pmatsci.2018.05.002>.
- [79] L. Lefebvre, J. Chevalier, L. Gremillard, R. Zenati, G. Thollet, D. Bernache-Assolant, A. Govin, Structural transformations of bioactive glass 45S5 with thermal treatments, *Acta Mater.* 55 (2007) 3305–3313, <https://doi.org/10.1016/j.actamat.2007.01.029>.
- [80] A. Riaz, K. Witte, W. Bodnar, M. Hantusch, N. Schell, A. Springer, E. Burkel, Structural changes and pseudo-piezoelectric behaviour of field assisted sintered calcium titanate, *Materialia* 15 (2021), <https://doi.org/10.1016/j.mtla.2021.100998>.
- [81] H. Cheng, H. Hu, G. Li, M. Zhang, K. Xiang, Z. Zhu, Y. Wan, Calcium titanate micro-sheets scaffold for improved cell viability and osteogenesis, *Chem. Eng. J.* 389 (2020), 124400, <https://doi.org/10.1016/J.CEJ.2020.124400>.
- [82] S. Yamaguchi, K. Akeeda, S.A. Shintani, A. Sudo, T. Matsushita, Drug-releasing gelatin coating reinforced with calcium titanate formed on Ti–6Al–4V alloy designed for osteoporosis bone repair, *Coatings* 12 (2022), <https://doi.org/10.3390/coatings12020139>.
- [83] G. Goller, H. Demirkiran, F.N. Oktar, E. Demirkesen, Processing and characterization of bioglass reinforced hydroxyapatite composites, *Ceram. Int.* 29 (2003) 721–724, [https://doi.org/10.1016/S0272-8842\(02\)00223-7](https://doi.org/10.1016/S0272-8842(02)00223-7).
- [84] M. Luginina, D. Angioni, S. Montinaro, R. Orrù, G. Cao, R. Sergi, D. Bellucci, V. Cannillo, Hydroxyapatite/bioactive glass functionally graded materials (FGM) for bone tissue engineering, *J. Eur. Ceram. Soc.* 40 (2020) 4623–4634, <https://doi.org/10.1016/j.jeurceramsoc.2020.05.061>.
- [85] H. Shokrollahi, F. Salimi, A. Doostmohammadi, The fabrication and characterization of barium titanate/akermanite nano-bio-ceramic with a suitable piezoelectric coefficient for bone defect recovery, *J. Mech. Behav. Biomed. Mater.* 74 (2017) 365–370, <https://doi.org/10.1016/j.jmbbm.2017.06.024>.
- [86] E.W. Yap, J. Glaum, J. Oddershede, J.E. Daniels, Effect of porosity on the ferroelectric and piezoelectric properties of (Ba_{0.85}Ca_{0.15})(Zr_{0.1}Ti_{0.9})O₃ piezoelectric ceramics, *Scripta Mater.* 145 (2018) 122–125, <https://doi.org/10.1016/j.scriptamat.2017.10.022>.
- [87] E. Fukada, Piezoelectricity in polymers and biological materials, *Ultrasonics* 6 (1968) 229–234, [https://doi.org/10.1016/0041-624X\(68\)90132-7](https://doi.org/10.1016/0041-624X(68)90132-7).
- [88] A.A. Marino, B.D. Gross, Piezoelectricity in cementum, dentine and bone, *Arch. Oral Biol.* 34 (1989) 507–509, [https://doi.org/10.1016/0003-9969\(89\)90087-3](https://doi.org/10.1016/0003-9969(89)90087-3).
- [89] E. Boccardi, A. Philippart, V. Melli, L. Altomare, L. De Nardo, G. Novajra, C. Vitale-Brovarone, T. Fey, A.R. Boccaccini, Bioactivity and mechanical stability of 45S5 bioactive glass scaffolds based on natural marine sponges, *Ann. Biomed. Eng.* 44 (2016) 1881–1893, <https://doi.org/10.1007/S10439-016-1595-5/FIGURES/8>.
- [90] H. Aguiar, J. Serra, P. González, B. León, Structural study of sol-gel silicate glasses by IR and Raman spectroscopies, *J. Non-Cryst. Solids* 355 (2009) 475–480, <https://doi.org/10.1016/j.jnoncrsol.2009.01.010>.
- [91] K. Zheng, A. Solodovnyk, W. Li, O.M. Goudouri, C. Stähli, S.N. Nazhat, A. R. Boccaccini, Aging time and temperature effects on the structure and bioactivity of gel-derived 45S5 glass-ceramics, *J. Am. Ceram. Soc.* 98 (2015) 30–38, <https://doi.org/10.1111/jace.13258>.
- [92] K. Lin, J. Chang, Z. Liu, Y. Zeng, R. Shen, Fabrication and characterization of 45S5 bioglass reinforced macroporous calcium silicate bioceramics, *J. Eur. Ceram. Soc.* 29 (2009) 2937–2943, <https://doi.org/10.1016/j.jeurceramsoc.2009.04.025>.
- [93] F.E. Cirraldo, E. Boccardi, V. Melli, F. Westhauser, A.R. Boccaccini, Tackling bioactive glass excessive in vitro bioactivity: preconditioning approaches for cell culture tests, *Acta Biomater.* 75 (2018) 3–10, <https://doi.org/10.1016/j.actbio.2018.05.019>.
- [94] J.P. Ball, B.A. Mound, J.C. Nino, J.B. Allen, Biocompatible evaluation of barium titanate foamed ceramic structures for orthopedic applications, *J. Biomed. Mater. Res., Part A* 102 (2014) 2089–2095, <https://doi.org/10.1002/jbm.a.34879>.
- [95] A.K. Dubey, G. Thirvikraman, B. Basu, Absence of systemic toxicity in mouse model towards BaTiO₃ nanoparticulate based eluate treatment, *J. Mater. Sci. Mater. Med.* 26 (2015), <https://doi.org/10.1007/s10856-015-5414-6>.
- [96] Z. Dong, X. Zhao, Application of TPMS structure in bone regeneration, *Eng. Regen.* 2 (2021) 154–162, <https://doi.org/10.1016/j.engreg.2021.09.004>.
- [97] C. Polley, W. Radlof, F. Hauschulz, C. Benz, M. Sander, H. Seitz, Morphological and mechanical characterisation of three-dimensional gyroid structures fabricated by electron beam melting for the use as a porous biomaterial, *J. Mech. Behav. Biomed. Mater.* (2021), 104882, <https://doi.org/10.1016/j.jmbbm.2021.104882>.
- [98] Z. Cai, Z. Liu, X. Hu, H. Kuang, J. Zhai, The effect of porosity on the mechanical properties of 3D-printed triply periodic minimal surface (TPMS) bioscaffold, *Bio-Design Manuf.* 2 (2019) 242–255, <https://doi.org/10.1007/s42242-019-00054-7>.